

SRESA's International Journal of

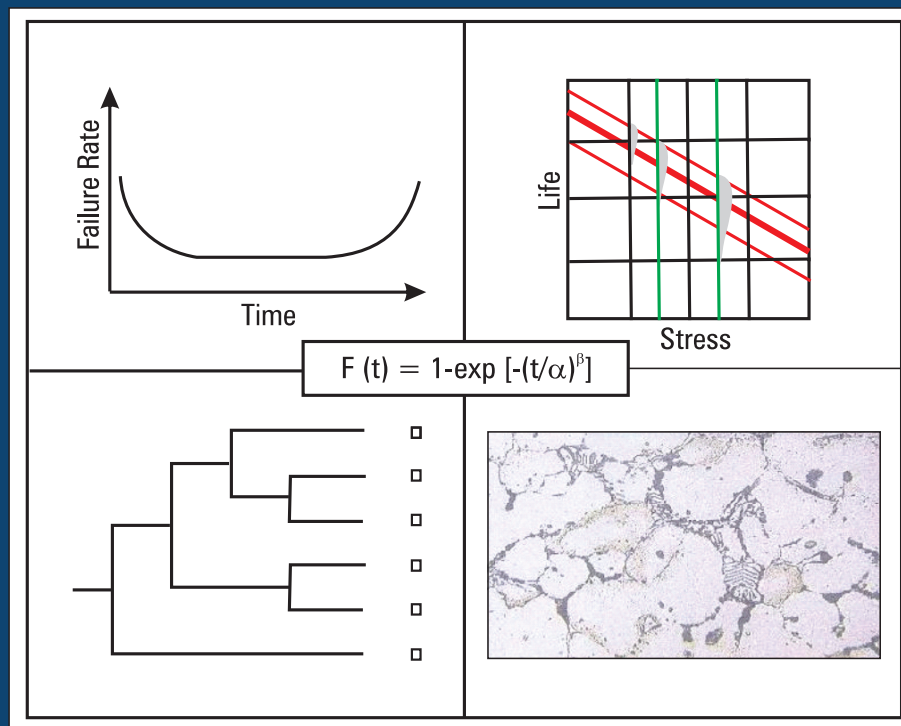
LIFE CYCLE RELIABILITY AND SAFETY ENGINEERING

Vol.5

Issue No.4

October-December 2016

ISSN – 2250 0820



Chief-Editors

P.V. Varde

A.K. Verma

Michael G. Pecht



Society for Reliability and Safety

website: <http://www.sresa.org.in>

SRESA Journal of Life Cycle Reliability and Safety Engineering

Extensive work is being performed world over on assessment of Reliability and Safety for engineering systems in support of decisions. The increasing number of risk-based / risk-informed applications being developed world over is a testimony to the growth of this field. Here, along with probabilistic methods, deterministic methods including Physics-of-Failure based approach is playing an important role. The International Journal of Life Cycle Reliability and Safety Engineering provides a unique medium for researchers and academicians to contribute articles based on their R&D work, applied work and review work, in the area of Reliability, Safety and related fields. Articles based on technology development will also be published as Technical Notes. Review articles on Books published in the subject area of the journal will also form part of the publication.

Society for Reliability and Safety has been actively working for developing means and methods for improving system reliability. Publications of quarterly News Letters and this journal are some of the areas the society is vigorously pursuing for societal benefits. Manuscript in the subject areas can be communicated to the Chief Editors. Manuscript will be reviewed by the experts in the respective area of the work and comments will be communicated to the corresponding author. The reviewed final manuscript will be published and the author will be communicated the publication details. Instruction for preparing the manuscript has been given on inside page of the end cover page of each issue. The rights of publication rest with the Chief-Editors.

SCOPE OF JOURNAL

System Reliability analysis	Structural Reliability	Risk-based applications
Statistical tools and methods	Remaining life prediction	Technical specification optimization
Probabilistic Safety Assessment	Reliability based design	Risk-informed approach
Quantitative methods	Physics-of-Failure methods	Risk-based ISI
Human factor modeling	Probabilistic Fracture Mechanics	Risk-based maintenance
Common Cause Failure analysis	Passive system reliability	Risk-monitor
Life testing methods	Precursor event analysis	Prognostics & health management
Software reliability	Bayesian modeling	Severe accident management
Uncertainty modeling	Artificial intelligence in risk and reliability modeling	Risk-based Operator support systems
Dynamic reliability models	Design of Experiments	Role of risk-based approach in Regulatory reviews
Sensitivity analysis	Fuzzy approach in risk analysis	Advanced electronic systems reliability modeling
Decision support systems	Cognitive framework	Risk-informed asset management

SRESA AND ITS OBJECTIVES

- a) To promote and develop the science of reliability and safety.
- b) To encourage research in the area of reliability and safety engineering technology & allied fields.
- c) To hold meetings for presentation and discussion of scientific and technical issues related to safety and reliability.
- d) To evolve a unified standard code of practice in safety and reliability engineering for assurance of quality based professional engineering services.
- e) To publish journals, books, reports and other information, alone or in collaboration with other organizations, and to disseminate information, knowledge and practice of ensuring quality services in the field of Reliability and Safety.
- f) To organize reliability and safety engineering courses and / or services for any kind of energy systems like nuclear and thermal power plants, research reactors, other nuclear and radiation facilities, conventional process and chemical industries.
- g) To co-operate with government agencies, educational institutions and research organisations

SRESA's International Journal of

LIFE CYCLE RELIABILITY AND SAFETY ENGINEERING

Vol.5

Issue No.4

October-December 2016

ISSN – 2250 0820

Chief-Editors

P.V. Varde

A.K. Verma

Michael G. Pecht



SOCIETY FOR RELIABILITY AND SAFETY

Copyright 2016 SRESA. All rights reserved

Photocopying

Single photocopies of single article may be made for personnel use as allowed by national copyright laws. Permission of the publisher and payment of fee is required for all other photocopying, including multiple or systematic photocopying for advertising or promotional purpose, resale, and all forms of document delivery.

Derivative Works

Subscribers may reproduce table of contents or prepare list of articles including abstracts for internal circulation within their institutions. Permission of publishers is required for resale or distribution outside the institution.

Electronic Storage

Except as mentioned above, no part of this publication may be reproduced, stored in a retrieval system or transmitted in form or by any means electronic, mechanical, photocopying, recording or otherwise without prior permission of the publisher.

Notice

No responsibility is assumed by the publisher for any injury and /or damage, to persons or property as a matter of products liability, negligence or otherwise, or from any use or operation of any methods, products, instructions or ideas contained in the material herein.

Although all advertising material is expected to ethical (medical) standards, inclusion in this publication does not constitute a guarantee or endorsement of the quality or value of such product or of the claim made of it by its manufacturer.

Typeset & Printed

EBENEZER PRINTING HOUSE

Unit No. 5 & 11, 2nd Floor, Hind Services Industries,
Veer Savarkar Marg,
Dadar (west), Mumbai -28
Tel.: 2446 2632/ 3872
E-mail: outwork@gmail.com

CHIEF-EDITORS

P.V. Varde,

Professor, Homi Bhabha National Institute &
Head, RRSD
Bhabha Atomic Research Centre, Mumbai 400 085
Email: Varde@barc.gov.in

A.K. Verma

Professor, Department of Electrical Engineering
Indian Institute of Technology, Bombay, Powai, Mumbai 400 076
Email: akvmanas@gmail.com

Michael G. Pecht

Director, CALCE Electronic Products and Systems
George Dieter Chair Professor of Mechanical Engineering
Professor of Applied Mathematics (Prognostics for Electronics)
University of Maryland, College Park, Maryland 20742, USA
(Email: pecht@calce.umd.edu)

Advisory Board

Prof. M. Modarres, University of Maryland, USA	Prof. V.N.A. Naikan, IIT, Kharagpur
Prof A. Srividya, IIT, Bombay, Mumbai	Prof. B.K. Dutta, Homi Bhabha National Institute, Mumbai
Prof. Achintya Halder, University of Arizona, USA	Prof. J. Knezevic, MIRCE Academy, UK
Prof. Hoang Pham, Rutgers University, USA	Dr. S.K. Gupta, Ex-AERB, Mumbai
Prof. Min Xie, University of Hongkong, Hongkong	Prof. P.S.V. Natraj, IIT Bombay, Mumbai
Prof. P.K. Kapur, University of Delhi, Delhi	Prof. Uday Kumar, Lulea University, Sweden
Prof. P.K. Kalra, IIT Jaipur	Prof. G. R. Reddy, HBNI, Mumbai
Prof. Manohar, IISc Bangalore	Prof. Kannan Iyer, IIT, Bombay
Prof. Carol Smidts, Ohio State University, USA	Prof. C. Putchu, California State University, Fullerton, USA
Prof. A. Dasgupta, University of Maryland, USA.	Prof. G. Chattopadhyay CQ University, Australia
Prof. Joseph Mathew, Australia	Prof. D.N.P. Murthy, Australia
Prof. D. Roy, IISc, Bangalore	Prof. S. Osaki Japan

Editorial Board

Dr. V.V.S Sanyasi Rao, BARC, Mumbai	Dr. Gopika Vinod, HBNI, Mumbai
Dr. N.K. Goyal, IIT Kharagpur	Dr. Senthil Kumar, SRI, Kalpakkam
Dr. A.K. Nayak, HBNI, Mumbai	Dr. Jorge Baron, Argentina
Dr. Diganta Das, University of Maryland, USA	Dr. Ompal Singh, IIT Kanpur, India
Dr. D. Damodaran, Center For Reliability, Chennai, India	Dr. Manoj Kumar, BARC, Mumbai
Dr. K. Durga Rao, PSI, Sweden	Dr. Alok Mishra, Westinghouse, India
Dr. Anita Topkar, BARC, Mumbai	Dr. D.Y. Lee, KAERI, South Korea
Dr. Oliver Straeter, Germany	Dr. Hur Seop, KAERI, South Korea
Dr. J.Y. Kim, KAERI, South Korea	Prof. P.S.V. Natraj, IIT Bombay, Mumbai
Prof. S.V. Sabnis, IIT Bombay	Dr. Tarapada Pyne, JSW- Ispat, Mumbai

Managing Editors

N.S. Joshi, BARC, Mumbai
Dr. Gopika Vinod, BARC, Mumbai
D. Mathur, BARC, Mumbai
Dr. Manoj Kumar, BARC, Mumbai

Physics Aspects of Adjuster Rod in Dhruva

Tej Singh, Paritosh Pandey, Jainendra Kumar, H. G. Gujar, P.V. Varde & S. Bhattacharya

Reactor Group, Bhabha Atomic Research Centre
Email: t_singh@barc.gov.in

Abstract

Cobalt based Adjuster Rod has been installed at G-19 lattice position, an important 150 KW unoccupied loop position, of Dhruva reactor. It was necessary to considerably reduce the minimum four days period generally required to bring the reactor at rated power from xenon free shut down state. It has, in turn, led to the enhancement of capacity factor, better utilization of fuel and improving the thermal safety margins due to increase in equilibrium moderator level. The design of adjuster rod has been optimized for the production of much needed high specific activity Co^{60} isotope for Teletherapy and many industrial applications. Introduction of adjuster rod was also important for enhancing the thermal neutron flux level by a factor of five at self serve facility required for short and medium duration exposures of Research & Development material studies. This article summarizes various physics aspects of recently commissioned adjuster rod assembly in Dhruva reactor core

Key words: Dhruva reactor, cobalt capsules, reactivity, argon activity, nuclear heating, temperature, shielding, reactivity worth of shutoff rods

1. Introduction

Dhruva is a 100 MW_{th} tank type thermal research reactor. It is fuelled with natural metallic uranium fuel with heavy water as coolant, moderator and reflector. Cross section of core layout is shown in Fig. 1.

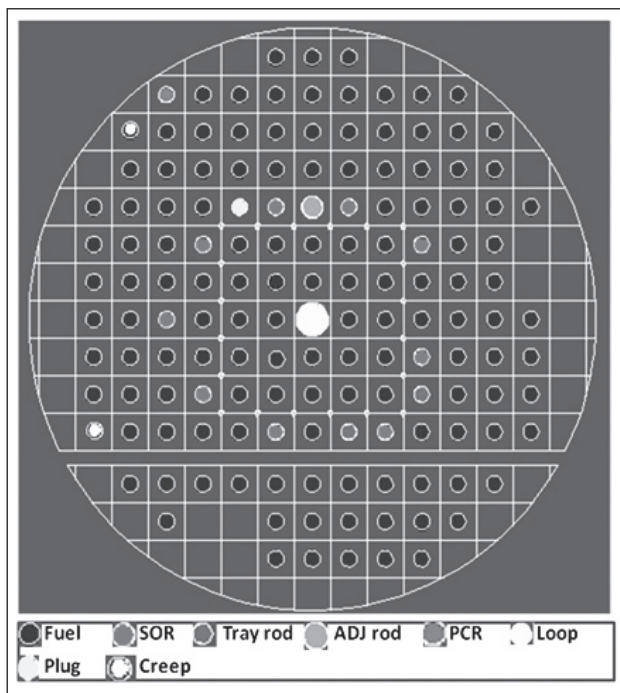


Fig.1: Dhruva core map

Co^{60} has been produced in Dhruva tray rod by irradiating 6 cobalt slugs (each with diameter 6 mm and length 25 mm) in regular capsules. However, the maximum cobalt activity is limited to 100 Ci/gm for dry handling and nuclear heating aspects. In order to achieve the desired high specific activity of 250-300 Ci/g, design of capsule for the adjuster rod has been optimized. The high specific activity can be obtained by increasing thermal neutron flux in the capsule. This can be achieved by either reducing diameter of the slugs to less than 4 mm or creating an annular gap of 2-3 mm for loading cobalt pellets instead of slugs to increase thermal neutron flux inside the target. Annular shape of capsule with cobalt in pellet form offers a very good design with low flux depression and better heat transfer geometry. In view of this, an adjuster rod with annular shaped cobalt capsules has been designed and installed at empty G-19 position of the reactor with insignificantly losing extra core excess reactivity. G-19 core position was chosen because of its location in highest flux position (i.e. near to the core centre) and it was being unutilized.

Installation of adjuster rod in Dhruva reactor also provides many operational aspect benefits. When the reactor is started-up from shutdown state, moderator level in the reactor vessel increases slowly due to buildup of xenon load and normally it takes more than four days to reach the rated power level. Thus, adjuster

rod assembly is very much needed for Dhruva type research reactor to bring the reactor power at rated level from shutdown state within two day which also increases capacity factor of the reactor significantly. In present scenario, design of adjuster rod with heavy water cooling is not possible due to the complexity involved such as removal of deck plate. Keeping this in mind, design of an air cooled adjuster rod assembly has been optimized for Dhruva reactor for adjustable reactivity load and high specific activity of Cobalt with adequate safety margins.

2. Design of Cobalt Filled Capsules

In the initial days of Dhruva reactor, design of adjuster rod was proposed with Li-Al as absorber material, and cooled by heavy water. But the same was not found feasible on account of requirement of reactor deck plate removal for installation of adjuster rod guide tube; the proposal was not pursued further. Considering this, it was decided to design an air cooled assembly for G-19 lattice position where air cooling can be provided without any complications. It was a very difficult task to commission an adjuster rod with air cooling for normal capsules due to requirement of very large coolant flow (8000 to 10000 slpm) which is not possible with existing air cooling facility. Thus, the present design of the adjuster rod has been arrived

at after detailed feasibility study for at least 4.0 mk adjustable reactivity load and thermal hydraulics analysis considering available air cooling capacity of less than 4500 slpm [1]. The design (see Figure- 2(a)) is based on annular shaped cobalt capsules loaded in movable tray section. The annular shaped capsule for the Adjuster Rod is made of two concentric aluminium tubes with 1.8 mm annular gap between the tubes. Inner & outer diameters of the capsule are 43 & 51.4 mm, respectively. Length of the capsule is 55 mm. The inner tube provides a central hole in the capsule of 43 mm diameter for passage of cooling air. Thus, the capsule gets cooling air on both inner as well as outer surfaces. Cross section area of normal and annular capsule is shown in Figure-2(b).

The annular gap of the capsule is filled with maximum 40 gm of cobalt pellets as target material. The capsules are held by spring clips on the Tray Section. The Tray Section is made of an aluminum

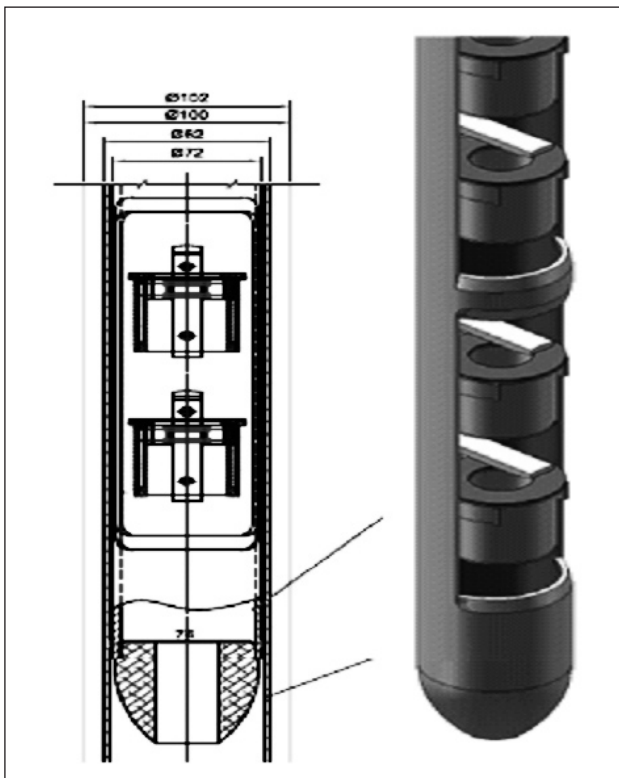


Figure 2(a): Regular and Annular Capsules

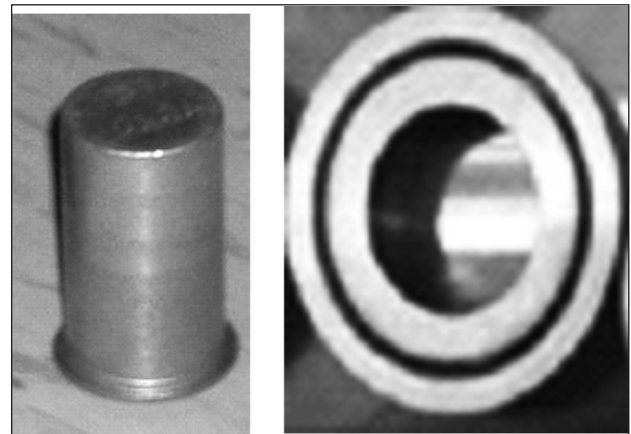


Figure-2(b): View of Capsules in Tray Section

tube of I.D. 66 & O.D. 68.4 mm. Total 10 nos. of identical windows (235 mm long and 62 mm wide) are cut on one side of the tube. Each window contains two pairs of spring clips to hold sample capsules at vertical gap of 50 mm. There are total 20 positions for sample capsules on the Tray Section. However, only 17 capsules filled with 35 gm cobalt in each capsule have been loaded in the tray section.

3. Physics Analysis

Physics design of the Adjuster rod was optimized for adjustable reactivity load, effect on critical moderator level & core power distribution, etc. Total reactivity loads of adjuster rod assembly for 35 and 40 gm of cobalt in each capsule have been calculated to 4.5 and 5.0 mk (including fixed load of 1 mk), respectively for 20 cobalt capsules. It is seen from the analysis that,

after installation of the Adjuster rod, the individual worth of SOR-1 & -3 near the adjuster rod are reduced from 12 and 13 to 10 and 11 mk, respectively due to shadowing effect of the adjuster rod. Combined worth of SORs without and with Adjuster rod are 118 and 116 mk respectively which meets Technical Specification requirements. The powers of central fuel channels in the neighborhood of G-19 are also reduced by 5-10 % which leads to flattening of core power distribution. Estimated thermal neutron flux level at self serve facility increases by a factor 5 which is better for irradiation of short and medium term isotope production without affecting the operation of the reactor. The increase in moderator level due to installation of adjuster rod will result in relatively flattened flux profile along the axial direction due to reflection of neutrons from top heavy water reflector. Axial peaking factor is estimated to reduce from 1.5 to 1.4 at 330 cm heavy water level resulting in lower thermal stress on the fuel assembly. Increase in equilibrium moderator level also leads to reduce by (i) maximum heat flux of a fuel assembly by 10 - 12% and (ii) peak to average burn up of a fuel assembly by about 10% keeping the discharge burn up same. Analysis indicates that the thermal neutron flux level at tiers above 300 cm will increase by a factor of two which will help in enhancing isotope production capacity.

Capacity factor of the reactor with adjuster rod is expected to be above 60%. Considering this, it is estimated that after 3 years of irradiation, the maximum specific activity will be about 300 Ci/g. Annual production of cobalt after first 3 years of irradiation will be about 50 - 60 KCi.

3.1 Radiological Aspects

The adjuster rod assembly consists of outer sheath, tray section, sample capsules, headgear, top shielding and bottom shielding. Prior to installation of the Adjuster rod assembly, detailed analyses for optimization of the shielding components using Monte Carlo method and point kernel method based computer codes were carried out. Shielding calculations for the adjuster rod have been carried out in two steps. In first step, gamma and neutron fluxes were estimated in the regions of the adjuster rod close to the reactor core i.e. below and above MS shield plug in the tray section and below the shield plug in the end shield region, by modeling 3D geometry of the reactor core using K-code mode of the Monte Carlo method based code. In the second step, shielding components were modeled in detail

using source mode of the Monte Carlo code with neutron and gamma fluxes obtained in the first step as source. Contributions from core gammas & neutrons and capture & decay gammas from cobalt capsules were considered appropriately. The photon and neutron flux values were used in Monte Carlo code for estimation of the source at top of pile. Radiation field at the top of pile after installation of the adjuster rod assembly is estimated to be about 27 mR/hr. Since the shielding calculation involves radiation streaming and transport over a length of about 5 meters, the results can vary by a factor of two.

It is estimated that due to the neutron activation of Argon present in the cooling air ~ 375 Ci of Ar^{41} is to be generated per day. The total release of Ar^{41} activity from the reactor will be ~1615 Ci/day which is less than the permissible value of 1620 Ci/day.

3.2 Thermal Hydraulic Aspects

Total heating in the adjuster rod assembly is estimated to be ~ 4.6 KW. Maximum nuclear heating produced in a cobalt capsule has been estimated to be about 130 watt.

The thermal calculation is done in three parts as mentioned below. a) The heat transfer calculation is done to calculate the maximum surface temperature of a capsule, which generates maximum nuclear heating. b) Calculation of Temperature of Tray section tube & Outer Sheath and heat losses (out of the AR system) - The temperature distribution for the tray section tube and outer sheath is found by performing finite element simulation considering different heat losses like, radiation, convection, and conduction. c) ΔT of flowing air was calculated considering different losses. Based on the ΔT_{air} , temperature of the capsule is estimated.

The heat generated in the annular capsule (Q_s) is transferred by two modes, which are convection ($Q_c = Q_{1c} + Q_{2c}$) and radiation (Q_{2R}). The heat transfer through radiation has been estimated to be about 5 Watt. The heat transfer coefficient for both the regions is calculated using Dittus-Boelter correlation as shown in Figure-3. For a trip value air flow rate of 3500 slpm at 3.5 atm pressure, the maximum surface temperature of the cobalt capsule is estimated to be 190 °C. The total amount of heat produced in the adjuster rod assembly is 4600 Watt, out of which, 800 watt of heat is lost out of the assembly through radiation and conduction. So, the heat of 3800 watt is picked by the cooling

air. The outlet air temperature with 3500 slpm flow rate has been calculated to be about 93 °C. Estimated maximum capsule surface and air outlet temperatures with nominal air flow rate of 4000 slpm are about 175 and 83 °C, respectively. The temperatures of the tray section tube and outer sheath are found to be about 73 and 125 °C, respectively. Nuclear heating produced from different components and maximum surface temperature of capsule in adjuster rod are given in Table-1 & 2.

Table-1: Nuclear Heating in Adjuster Rod

Components	Nuclear Heating (KW)	
	40 g Cobalt in a Capsule	35 g Cobalt in a Capsule
18 Capsules	2.1	1.85
Tray Section	0.7	0.65
Outer Sheath	1.6	1.6
Others	0.5	0.5
Total	4.9	4.6

Table-2: Max. Capsule Surface Temperature with Nominal and Trip Value Flow Rates

Capsule Heating in Watt	Air Flow (slpm)	H _{eff} in W/m ² /K	Capsule Surface Temp (°C)
131 (35 g)	4000	72	175
131 (35 g)	3500	66	190
150 (40 g)	4000	72	189
150 (40g)	3500	66	206

3.3 Safety Analysis

The adjuster rod will be normally raised during reactor startup to override xenon poisoning. Loss Of Regulation Incident (LORI) analysis has been carried out wherein simultaneous withdrawal of adjuster rod and uncontrolled pump-up of heavy water is assumed. The transient is assumed to be initiated from two different power levels of 1 kW and 100 MW. Maximum withdrawal speed of 2 cm/sec has been considered for the analyses.

The equilibrium heavy water level at 1 kW power is assumed to be 200 cm. With adjuster rod down, minimum moderator level will be about 210 cm to keep minimum shut down margin of 50 mk. The reactivity addition rate at this level due to uncontrolled pump-up of heavy water and uncontrolled withdrawal of adjuster rod together is estimated to be about 0.33 mk/sec.

As per 32.5 MW/m rule, the minimum equilibrium heavy water level at 100 MW power is about 308 cm. The reactivity addition rate at this level due to uncontrolled pump-up of heavy water and uncontrolled withdrawal of adjuster rod is about 0.15 mk/sec. Results are summarized in Table-3.

Table-3: LORI Results at 1 KW&100 MW

Parameters (unit)	LORI at 1 KW	LORI at 100 MW
Reactivity rate (mk/s)	0.33	0.15
Trip at 110 MW (s)	23.10	9.60
Peak Power (MW)	157.8	133.9
Max. reactivity add (mk)	7.86	1.05
Max. log rate (%/s)	143	3.5
Max. fuel temp. (°C)	635	460
Max. clad temp. (°C)	221	189
Max. coolant temp. (°C)	102	113

On failure of air compressors, the reactor will trip as soon as the pressure comes down to 5.4 Kg/cm²

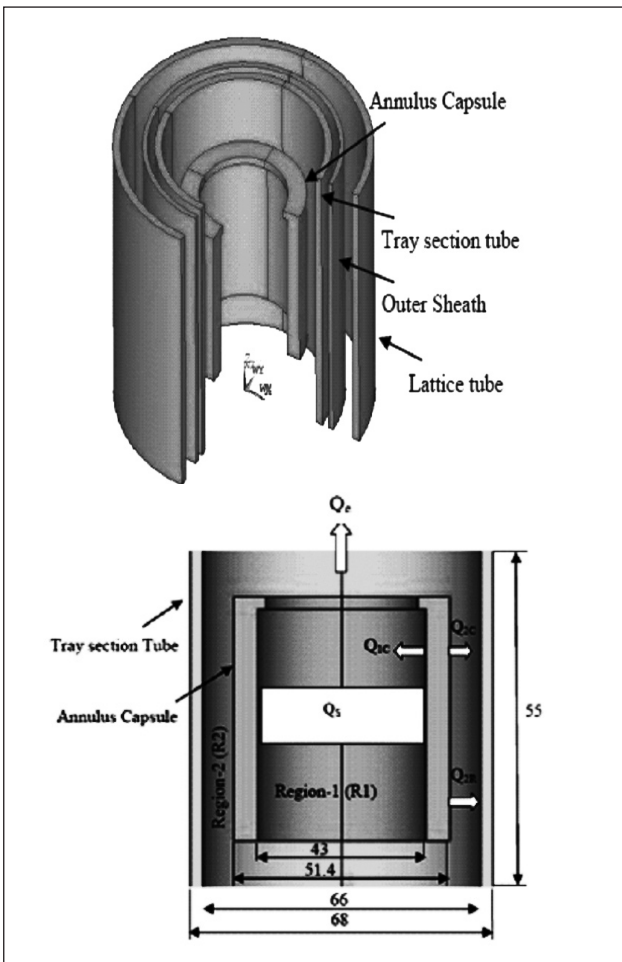


Fig.3: Geometry of Annular Capsule

from normal value of 7.8 Kg/cm². For cobalt capsules with specific activity of 300 Ci/g, the decay heat is ~ 18 Watt for which the surface temperature of the capsule stabilizes at ~320°C. The conditional trips on air flow and pressure are effective only at power above LP. At LP, total heat deposition in the capsule from decay and core gamma will be ~ 20 Watt. For nominal air flow of 4000 slpm, the capsule surface temperature and air outlet temperature will be 68 and 42°C, respectively at LP. If air flow through the adjuster rod stops when reactor is at LP, surface temperature of the hottest cobalt capsule reaches maximum up to 350°C.

4. Observations

Important physics parameters were measured after commissioning of Adjuster rod, and comparison with estimated values are summarized in Table-4.

The reactivity worth calculation of all nine shut off rods with adjuster rod IN was carried out using inverse kinetics method.

At low power, however, proper estimation of source term (S) is necessary to get correct value of reactivity. If the source term is unknown, we proceed using the method developed by Hoogenboom [2].

Once full worth of the shut off rods, ρ_d is realized, its relationship with constant source term is given by: $\rho_d = \rho_j - \Delta S / \eta_j$. Here, ρ_j is reactivity calculated from inverse point kinetics with source term taken as zero, and η_j is reactor power or equivalent. Above equation is linear in form. To estimate ρ_d , least squares approximation for ρ_j and η_j can be made. This method for determining the post-scrum reactivity is called Least Squares Inverse Kinetics Method (LSIKM).

The reactor was initially made critical at low power (LP), and fast recorder with scan time of 1 msec was connected to record log power signal.

5. Concluding Remarks

The adjuster rod is much needed for Dhruva type research reactors. The adjuster rod installed

Table-4: Estimated & Observed Values of Important Parameters with Adjuster Rod

Parameter	Estimated Values	Observed Values
Reactivity load	4.3 mk	4.2 mk
Fixed load	1.0 mk	~1.0 mk
SORs worth	118 mk	116 mk
Peak Power	1132 kW	1133 kW
Ar ⁴¹ release	375 Ci/day	365 Ci/day
Radiation field at top of pile	27 mR/hr	35 mR/hr
Max. ϕ_{th} in Self Serve facility	1.5x10 ¹³ n/cm ² /sec	1.54x10 ¹³ n/cm ² /sec
Outlet Air temp.	83°C	79 °C

at G-19 position, consists of 18 cobalt capsules with 35 g of cobalt in each capsule. The adjuster rod has total reactivity load of 4.3 mk with 3.3 mk adjustable. Thermal safety margins and shielding analysis for adjuster rod assembly demonstrate adequate safety margins. The estimated results for reactor physics, thermal hydraulics and radiation shielding are in close agreement with the observed values.

Acknowledgements

We are thankful to Shri R.C. Sharma, Ex. Director Reactor Group for his keen interest. We are also thankful to the core team of Operation, Maintenance and Servicers. The authors also thank Shri Manoj Tilara, Head, SRC, RRMD and CDM for the fabrication work.

Reference

1. "Physics & shielding design and safety analysis of Adjuster rod in dhruva", BARC/2016/I/007, 2016
2. "Neutron source strength determination for on-line reactivity measurements", J.E. Hoogenboom, A.R. van der Sluijs, Annals of Nuclear Energy, 15 (12) 1988, pp 553-559.

Estimation of Fatigue Model Parameters For PLCC Solder Joints Under Thermal Cycling

Rohit Khatri¹, Diana Denice², Manoj Kumar², P.P.Marathe²

¹Homi Bhabha National Institute, Anushaktinagar, Mumbai

²Control Instrumentation Division, Bhabha Atomic Research Centre, Mumbai

Email: dianad@barc.gov.in

Abstract

Electronic system reliability is always limited by reliability of its components and solder joints. Over the years, component reliability has improved because of improvement in manufacturing technology. Nevertheless solder joint reliability can be a limiting case and early solder joint failure may hamper system reliability. Therefore, estimation and insurance of solder joint reliability is an important activity to ensure system reliability goals.

Plastic Leaded Chip Carrier (PLCC) package comes with J-leads and the solder joint geometry is quite unique. For lead solder joints of this package life estimation models are not available in literature. Considering the fact that thermal cycle is the most predominant stress for electronic systems, causing fatigue failure of solder joints, thermal cycling experiments has been used for estimation of life of the solder joints. Parameters of Coffin-Manson model is estimated from the experimental data. With this a specific life model is derived for PLCC solder (lead) joints.

Keywords: Solder joints, thermal cycle, Fatigue life, Finite element, Accelerated life testing

1. Introduction

Solder joints form a vital part of electronic systems. Their role is to provide i) electrical inter-connect ii) mechanical bond iii) thermal conduit for removal of heat. Over the years, component reliability has improved because of improvement in manufacturing technologies. However, solder joint reliability can be a limiting case and early solder joint failure may hamper system reliability. Therefore, estimation of solder joint reliability is critical to ensure system reliability goals. Also, extensive studies have shown that 25% of all

hardware failures in electronic systems are due to solder joint failures [1] as shown in Fig. 1.

Electronic components come in various packages such as DIP, BGA, and PLCC etc. For each of these packages, solder joints take a different geometry. Solder joint reliability depends on solder material, their microstructure and geometry, in addition to environmental factors [2]. As a result, a universal model for reliability/life estimation of each type of solder joint is not possible.

Plastic Leaded Chip Carrier (PLCC) package components have been extensively used in concurrent designs. These components come with J-leads and the solder joint geometry is quite unique. The solder material used in these designs is Sn-37Pb, i.e. lead solder. In literature solder joint life models are available for some packages with solder (lead) joints. With RoHS (Restriction of Hazardous Substances) directive in force, most of the research has focused on leadless solder joints. This has created a gap area for PLCC solder (lead) joints.

Environmental factors that greatly influence the life of solder joints include temperature, thermal cycling, vibration, shock etc. Each of them accelerates a

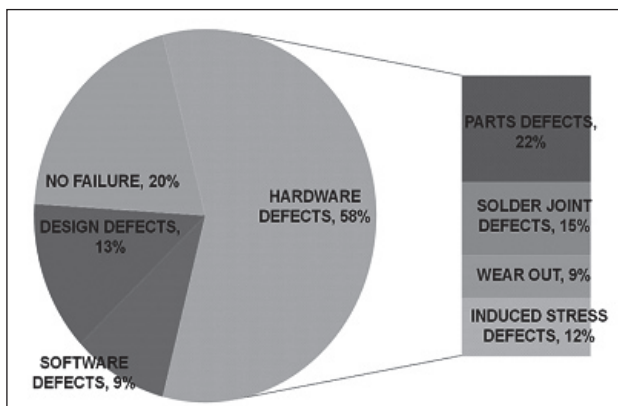


Fig. 1: Failure causes distribution of an electronic system

failure mechanism in the solder material causing them to fail. In this work, thermal cycling stress has been chosen to estimate life of PLCC solder joints due to its predominance in the actual use environment. Since, fatigue is the dominant failure mechanism under thermal cycling, it has been considered for estimation of solder joint life. Thermal cycling experiments have been used in the paper for life estimation.

Section 2 gives a background on fatigue mechanism in general and reviews solder joints of electronic components. Section 3 specifies the fatigue mechanism in solder joints and the model for fatigue. Section 4 details the Finite element modelling of PLCC solder joints. In section 5, planning and conduct of accelerated thermal cycling experiments is given. Finally, section 6 shows the estimation of fatigue model parameters.

2. Background

2.1 Fatigue

It is known that all materials are subjected to degradation & ageing with time & environment. A solder joint can be termed as failed if cracks have developed forming discontinuities. The three main causes of solder joint failure as per literature [2] are:

- i) Fracture: Mechanical overloading due to tensile rupture
- ii) Creep: Damage due to long-lasting permanent loading at elevated temperature
- iii) Fatigue: Damage due to cyclic loading

Fatigue failure is defined as a process causing localized, progressive and permanent micro-structural damage when the material is subjected to fluctuating stresses and strains at some material point or points [4]. It occurs under alternating stresses, causes failure when the maximum operating stress is of sufficiently high value, or there is enough variation of the applied stress or even if there is a sufficiently large number of stress cycles. Sooner or later, it leads to crack initiation and propagation and finally failure [2].

To quantify fatigue life, empirical fatigue life models are available in literature [3]. Widely used models are Coffin-Manson, Total strain, Solomon, Engel Maier etc. These models are based on plastic strain due to thermal cycling and/or vibration loading for a given environmental conditions.

2.2 Solder Joints

Solder joints microstructure and geometry coupled with environmental conditions significantly affect

their life. The geometry of solder joints varies with different component packages. For BGA packages, it takes a spherical shape while for PLCC packages, it takes an M shape. Since solder joint life greatly depends on geometry, it is imperative to evaluate life of individual type of solder joints.

Solders are classified into lead and leadless ones based on the presence or absence of lead (*Pb*). *Sn-37Pb*, *Sn-3.5Ag-3Bi* are examples of lead and leadless materials, respectively. Implementation of *RoHS* (Restriction of Hazardous Substances) directive imposed restriction on the use of *Pb* in the industry. Ever since, leadless solders gained the market and current research is also in line with that. As a result, life data is not available for solder joints with lead solder material, for concurrent package.

The electronics for critical applications, such as NPP, avionics and space, still uses lead solder joints due to their well-known behaviour and established reliability. The paper attempts to fill this gap for lead solder joints of PLCC packages.

3. Fatigue Life of Solder Joints

3.1 Fatigue Mechanism due to Thermal Cycling

Fatigue caused by thermal cycling is categorized as a low cycle fatigue (LCF) phenomenon. That is, the number of cycles to failure is less than 10^4 cycles. The fatigue occurs due to mismatch in coefficients of thermal expansion (CTE) between the component leads, solder and the PCB [3]. On repeated exposure to thermal cycling, these materials expand and contract differently due to CTE mismatch. This induces plastic strain or deformation in the solder joint, culminating in crack initiation and further growth.

For fatigue life due to thermal cycling Coffin-Manson model is well accepted. Here also, Coffin-Manson is adopted as it considers only plastic strain, which is the main contributor for failure in case of thermal cycling.

3.2 Fatigue Model

Coffin-Manson fatigue model [3] is the most widely used fatigue model for plastic strain based LCF. The total number of cycles to failure (N_f) is dependent on the plastic strain range ($\Delta\varepsilon_p$), the fatigue ductility exponent (c) and the fatigue ductility coefficient (ε_f). It is expressed by,

$$\Delta\varepsilon_p = \varepsilon_f' (2N_f)^c \quad (1)$$

Where,

$\Delta\varepsilon_p$: plastic strain range.

ε_f : fatigue ductility coefficient, defined as the failure strain for a single reversal ($2N_f = 1$).

$2N_f$: number of reversals to failure.

c : an empirical constant also known as the fatigue ductility exponent. It depends on the material and its geometry.

From Eqn. (1), it can be seen that $\Delta\varepsilon_p$, ε_f and c need to be obtained for concerned solder joints to estimate N_f .

Due to the small size of solder joints, traditional methods of strain measurements such as strain gauges cannot be used. Literature suggests the use of Finite Element method for solder joints to estimate strain ranges. To estimate other model parameters, it is also necessary to estimate number of cycles to fatigue failure by accelerated testing. Details of the test sample, sample size, temperature ranges and acceleration life tests are given in the Appendix.

4. Finite Element Analysis (FEA) of PLCC solder-joint

PLCC solder joint under study is modelled using Finite element model. Through this method, $\Delta\varepsilon_p$ is estimated. Step-up step procedure for FE analysis is given below.

4.1 Assumptions in FEA

Assumptions for FE (Finite Element) analysis are as follows.

- All the parts in package are assumed to be perfectly bonded to each other.
- Temperature change and displacement is assumed to be uniform throughout.
- Except solder joints, all other materials are assumed to behave as linear elastic.
- No material is considered to possess time varying material properties.

Fig 11 indicates that sample is symmetrical in both axes, so a quarter model can be used. A quarter model possesses symmetry in boundary conditions and applied loadings. This helps in reducing the size of the model, hence the computation time, without affecting the results.

4.2 FEA model

The geometry of the package used for FEA is given in Fig. 2a & 2b.

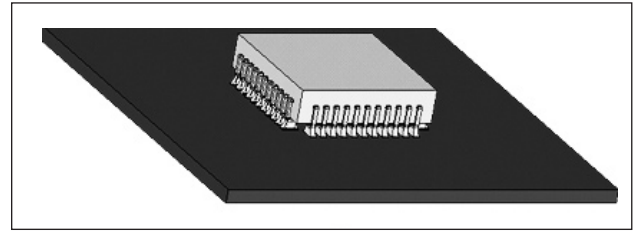


Fig 2a: Complete FE model

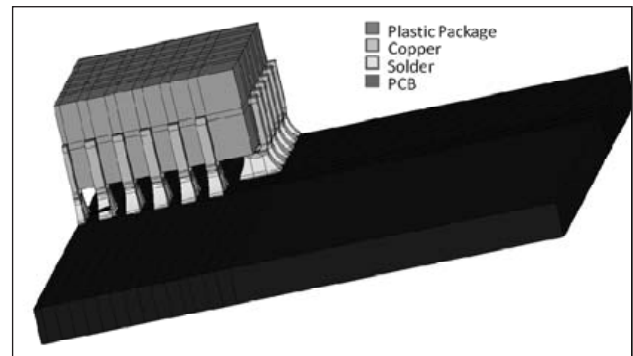


Fig 2b: Quarter model

Fig. 2a is the complete FE model while Fig. 2b shows the quarter model of PLCC package test assembly.

Copper (Cu) pads, J-leads, plastic package encapsulation and PCB are modelled as linearly elastic materials. Sn-37Pb solder is modelled as elastic-plastic material with yield strength of 27.23 MPa. The material properties for the model are extracted from standard references [6, 7] and are listed in Table 1 and 2.

Table 1: Mass of Materials of Sample Package

Material	Mass (gms)
Plastic Package	2.44 (with J-leads)
PCB	8.43

Table 2: Material Properties used in FEA

Material	CTE (ppm/°C)	Elastic Modulus (GPa)	Poisson Ratio	Density (kg/m ³)
Copper pad and Leads	16.7	117	0.35	8940
Plastic Package	22	13.79	0.30	1800
PCB	18	22	0.28	2200
Sn-37Pb Solder	24.7	15.7	0.4	8500

Once the model is ready, the next step is to mesh it with finite elements. The size of elements and the degree of interpolation function chosen for the elements affect the accuracy of field variables such as displacement etc. Fine sized element mesh could ensure high accuracy of the FE results [8].

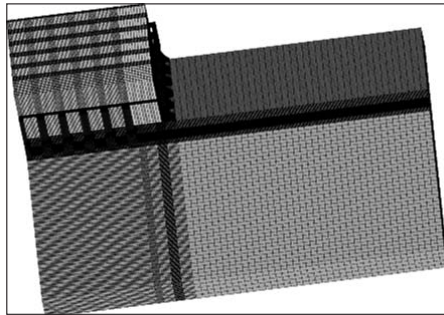


Fig 3: Meshing of quarter model

The meshed geometry of the quarter model is presented in Fig. 3. Mesh density is made higher in solder joint volumes (area of interest) for accurate results and intentionally rarer at other areas so as to save on computational time.

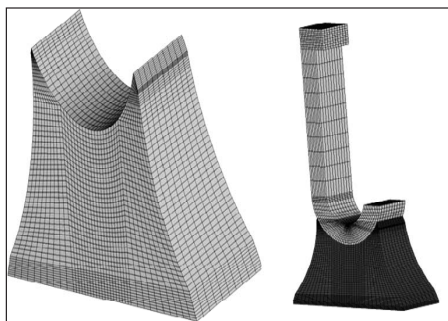


Fig 4: Solder joint & J-lead with solder joint

The quarter model in Fig. 2b consists of 739965 nodes and 140694 elements with 3D SOLID 186 elements. A more detailed view of the meshed geometry of the solder joint and J-lead is presented in Fig. 4.

4.3 FEA Results

On simulation, the plastic strain range $\Delta\varepsilon_p$, induced per cycle in solder joints for ALT I and ALT II (refer to Appendix for thermal loading profile) are summarized in Table 3.

Table 3: ALT Results

Test	$\Delta\varepsilon_p$
FEA-ALT I	0.014983
FEA-ALT II	0.011909

Fig. 5 and 6 show the plastic strain induced (light blue colour) in solder joints in ALT I & II respectively.

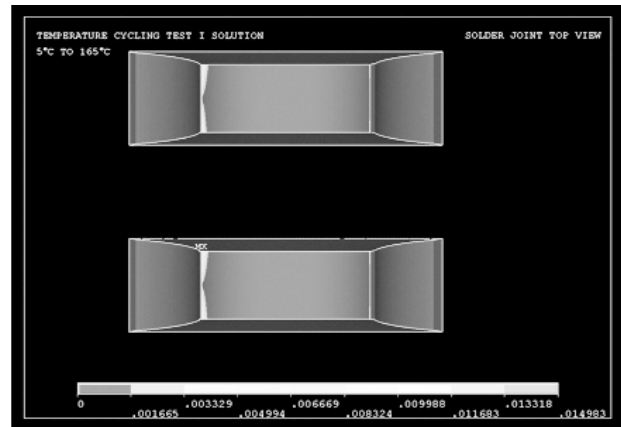


Fig 5: Plastic strain in solder joints for ALTI

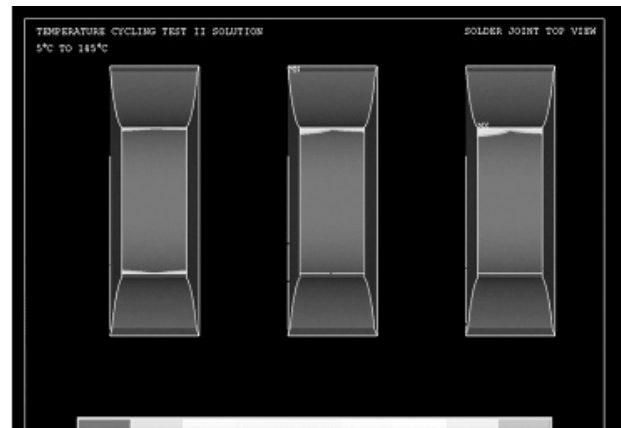


Fig 6: Plastic strain in solder joints for ALTII

Red colour in the colour bar indicates the highest strain area followed by orange, yellow etc.

As visible in the figures, largest strains occur at the outer edges of the solder volume; at the interface of the J-lead and solder. It is due to higher stiffness of the J-lead at the outer side compared to the inner side where its one end is free.

5. Experiment

5.1 Experimental Setup

The test set up as shown in Fig. 7, consists of two thermal chambers maintained at 165 °C and 145 °C respectively. The cold temperature of 5 °C was achieved using a water bath. The samples were manually cycled between the two chambers in accordance with the cycling profile. An average of 12 cycles/day was achieved.



Fig 7: Thermal cycling chamber & water bath

5.2 Pre-experiment Defect Analysis

Visual inspection aided by magnification between 4X to 10X and use of additional magnification to resolve suspected defects is a reliable and widely used method [9] to detect solder joint failures.

Following methods were employed for presence of cracks and thus identification of failure of solders joints:

- Stereo Microscope imaging of the sample.
- Resistance measurement of solder joints using Low Resistance measurement facility (100 nΩ to 2 Ω)

Stereo Microscope Images of the samples prior to commencement of experiments are shown in Fig. 8. As seen from the images, all the joints are healthy.

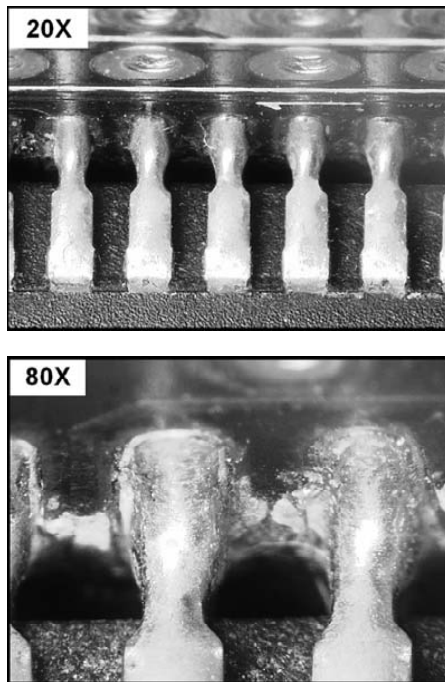


Fig 8: Stereo microscope images showing crack-free solder joints

Resistance of all individual solder joints at the start of experiment were also recorded. The range of resistance for healthy solder joints (including component leads) was found to be varying between 105 mΩ to 120 mΩ.

Both the methods mentioned here are offline techniques; hence samples were removed from the test at regular intervals for monitoring.

5.3 Thermal Cycling Experiment

Two thermal tests are conducted keeping the same loading conditions as FEA. More details can be found in [10].

5.4 Results

Results of conditions ALT I and ALT II are tabulated in Table 5.

Table 4: Cycles to Failure for ALT I & II

Experiment	N_f
ALT I	255
ALT II	375

The first defect was observed at 200th cycle for ALT I conditions and 325th cycle for ALT II conditions. The tests were terminated at 255 cycles for ALT I and 375 cycles for ALT II conditions for 50% solder joint failures.

Fig. 9 shows the stereo microscope images of the cracks occurred in ALT I and ALT II test conditions at the end of cycling.

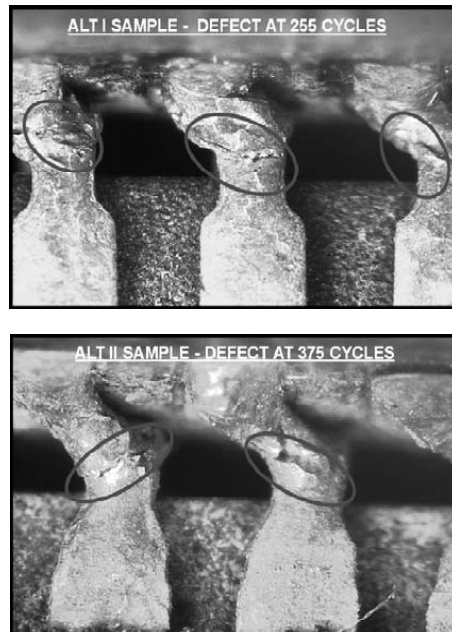


Fig. 9: Cracks observed in samples of ALT I & II

Some additional observations of the experiments are as follows:

1. The location of the crack, as seen in Fig. 9 was on the outer side of the interface, between solder joint and J-lead. This is clearly in line with the results of FEA, which indicated the very same region with maximum plastic strain.
2. The resistance of individual solder joints with defects was observed to vary from 245 mΩ (in case of small cracks) to 2 Ω (for cracks spread throughout the volume).
3. It was also observed that the change in resistance of the corner solder joints (Pin no. 1, 11, 12, 22, 23, 33, 34 and 44) was the greatest (greater than 2 Ω). Thus, the corner solder joints for a PLCC package are the critical solder joints under thermal cycling loading.

6. Estimation of model parameters

The objective of the study is to estimate fatigue model parameters for thermal loading of J-lead solder joints of PLCC package, with lead solder material. The results from experiment and FEA are used for estimation of fatigue model parameters.

6.1 Parameter for Coffin-Manson (LCF) Model

Results from experiment (N_f) and FEA (plastic strain range) for thermal cycle load are summarised in Table 5. These are used to estimate parameters of Coffin-Manson model.

Table 5: Temperature Cycling Loading Results

	N_f	$\Delta\epsilon_p$
ALT I	255	1.4983%
ALT II	375	1.1909%

From literature [6, 11], ϵ_f' is taken as 0.65 for Sn-37Pb solder material. Therefore the Eqn. (1) can be written in log form as:

$$\log(\Delta\epsilon_p) = \log(0.65) + c \log(2N_f) \tag{2}$$

Eqn. (2) clearly indicates a linear relationship between logarithm of $2N_f$ and $\Delta\epsilon_p$. From Table 5, values of N_f and corresponding $\Delta\epsilon_p$ for two ALT levels are available. Single reversal ($2N_f=1$) forms the 3rd data point. Data points are summarized in Table 6.

Table 6: Data Points for Regression Analysis for Estimation of c

Data Point	$x = \log(2N_f)$	$y = \Delta\epsilon_p$
A	0	-0.4881
B	2.7076	-1.8244
C	2.8751	-1.9241

The slope of best fit line is nothing but the value of c.

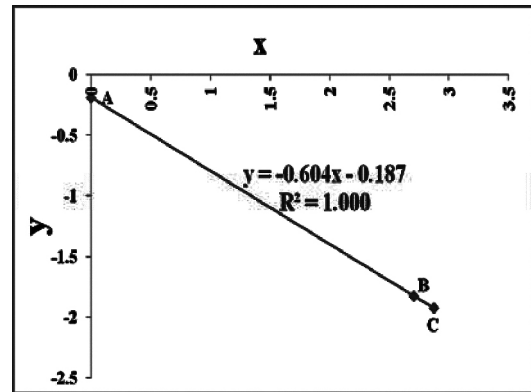


Fig. 10: Regression plot to estimate c

From the regression plot shown in Fig. 10, c is estimated to be -0.604, which lies within the specified range (-0.5 to -0.7) [3]. Thus, the fatigue model for PLCC (with J-lead and Sn-37Pb solder) solder joints under temperature cycling can be expressed as:

$$\Delta\epsilon_p = (0.65)(2N_f)^{-0.604} \tag{3}$$

7. Conclusion

General empirical models for estimation of fatigue life are available in literature. These models have parameters which are function of geometry and material. In the paper, parameters of Coffin-Manson model for PLCC solder joint with Sn-37Pb solder material under thermal cycle loading are estimated. FE models were used to estimate the strain range. The results of strain analysis indicate highest strain at the outer edge of the package and the corner pins of the package.

The specific fatigue model for PLCC solder joint can be used for predicting the life in use environment as part of overall system reliability estimation. It will also be useful in deciding the need of environmental control and estimation of Remaining Useful Life (RUL).

Acknowledgement

The work presented here requires support of a number of tools and test setups. We got active

support from experts of various divisions of BARC for different activities. To name a few – Shri Deependra Singh, RRDPD for FE analysis; Shri Sanjay Kumar, Shri N. Saikathik, Dr. R. Tiwari and Dr. V. Kain of MSD for SEM and stereo imaging; Shri N.B. Shrestha and Shri P.K. Ramateke of RSD for thermal cycling experiments; and Shri P. Trivedi, ACnD for resistance measurement. We thank all for their kind support and making this work possible.

References

1. Milton Ohring, *Reliability and Failure of Electronic Materials and Devices*, Academic Press Publication, 2014
2. Johan Liu, *Reliability of Micro technology: Interconnects Devices and Systems*, Springer Publications, 2010
3. Lee, W. W., L. T. Nguyen, and Guna S. Selvaduray, "Solder joint fatigue models: review and applicability to chip scale packages." *Microelectronics Reliability*, Vol 40 (2), pp. 231-244, 2000.
4. L. Anand and D. M. Park, *Mechanics and Materials: Supplementary Notes*, Massachusetts Institute of Technology, 2004.

5. Zilog Product Specification Z8536 Counter/Timer and Parallel I/O Unit. URL: http://www.zilog.com/appnotes_download.php.
6. IPC SM 785, Guidelines for Accelerated Reliability Testing of Surface Mount Solder Attachments, IPC, 1992.
7. Siewert, Thomas, Stephen Liu, David R. Smith, and Juan Carlos Madeni, "Database for solder properties with emphasis on new lead-free solders." *NIST & Colorado School of Mines, Release 4*, 2002.
8. Tamin Mohd and Norhashimah Shaffiar, *Solder Joint Reliability Assessment: Finite Element Simulation Methodology*, Springer Publications, 2014.
9. Fox, L., J. Sofia, and M. Shine, "Investigation of solder fatigue acceleration factors" *IEEE transactions on components, hybrids, and manufacturing technology*, Vol. 8 (2), pp. 275-282, 1985.
10. Rohit Khatri, *Estimation of Fatigue life of PLCC solder joints due to vibration and thermal cycling*, M. Tech. Thesis, HBNI, 2016
11. Norris, K. C., and Landzberg, A. H., Reliability of controlled collapse interconnections. *IBM Journal of Research and Development*, Vol. 13 (3), pp. 266-271, 1969.
12. Pecht Michael, *Integrated Circuit Hybrid and Multichip Module Package Design Guidelines: A Focus on Reliability*, Wiley and Sons Publication, 1999.

APPENDIX

Description of Test Samples and Thermal Cycles

A-1 Test Sample

For both FEA and experimentation, sample under consideration is a 16.5 x 16.5 x 4.3 mm PLCC package mounted on 48 x 48 x 1.6 mm PCB as shown in Fig. 11. Four samples were cut out from a single 6U size module.

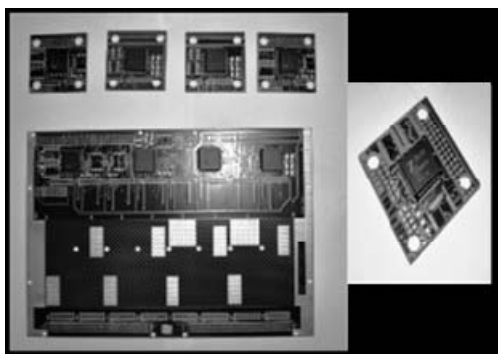


Fig.11: Test sample

This PLCC package has 44 J-leads for solder joints. Solder material is Sn-37Pb. Hence, solder joints sample size available is 44, which is statistically a good size. More details on the same can be obtained from [10]. The details of the samples are summarized in the Table 7.

Table A-1: Dimensions of FEA Model Geometry

Component	Dimension (mm)
PCB	48 x 48 x 1.6
PLCC Package	16.5 x 16.5 x 4.3
Copper Pads	0.65 x 2
Solder Joint Height	0.762
Stencil Size	0.60 x 1.95

A-2 Thermal Cycles

IPC-SM-785 [6] provides recommended accelerated testing levels for surface mounted electronics. The standard also prescribes that the rate of change of temperature should be less than 20°C/min to avoid thermal shock. Usually for experiments higher stress levels (range of thermal cycles) are chosen to reduce the experimentation time.

Two stress levels chosen for carrying out temperature cycling are:

- i) ALT I: Cycling between 5 °C and 165 °C.
- ii) ALT II: Cycling between 5 °C and 145 °C.

These conditions ensure acceleration of the fatigue mechanism and are well below the solder melting point to avoid shifting of active failure modes.

In Fig 12, dotted lines depict the thermal cycle profile used in Finite element analysis while the solid line profile is used in experiments. Due to the limitation of the thermal chambers, the ideal dotted line could not be achieved for experiments. Thermal cycling conditions employed are summarised in Table 8.

Table A-2: Thermal Cycle Profile for FEA and Experiments

Parameters	FEA	ALT I	ALT II
Cycle duration	40 min	40 min	40 min
Dwell time	10 min	20 min	20 min
Ramp rate	16°C/min	16°C/min	14°C/min

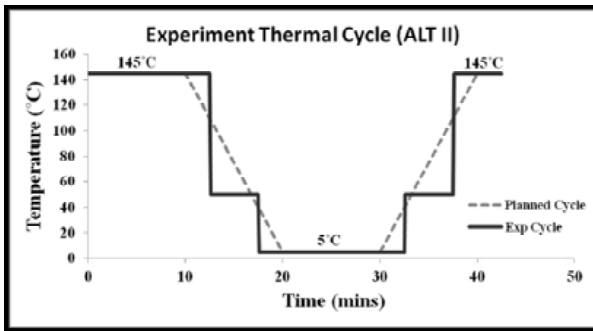
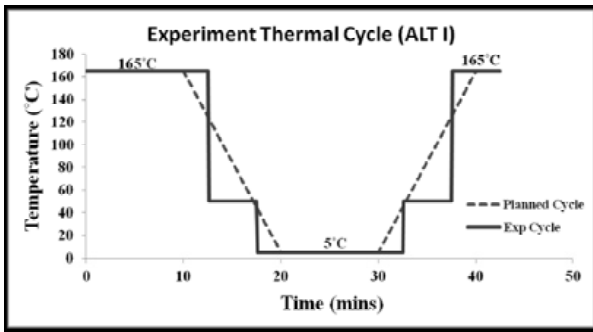


Fig. 12: Actual profile for ALT I & ALT II

A-3 Estimation of Acceleration Factor and Test Duration

While conducting any experiment, test duration must be determined a priori. The most common approach in accelerated life testing is to use an AF (Acceleration Factor) model, operating stress & accelerated stress to calculate the expected cycles to failure at accelerated conditions.

Norris-Landzberg equation gives estimation of Acceleration Factor [11] for thermal cycling as

$$AF = \left(\frac{N_{field}}{N_{test}} \right) = \left(\frac{N_{field}}{N_{test}} \right)^{-m} \left(\frac{\Delta T_{field}}{\Delta T_{test}} \right)^{-n} e^{\left(\frac{E_a}{K} \left(\frac{1}{T_{field}} - \frac{1}{T_{test}} \right) \right)} \quad (4)$$

Where,

E_a : Activation energy

K : Boltzmann constant

m, n : Parameters for material

Values for m, n, E_a have been taken for Sn-37Pb eutectic solder from [11]. Operating environment cycling range is 5°C to 45°C at one cycle per day. Test conditions for ALT I and II are already specified. Ref. [12] also provides the use life of lead solder joints (N_{test}) as 35000 cycles.

Using eqn. (4) the Acceleration factors and thus estimates of number of test cycles required at test levels ALT I and ALT II are given in Table 9.

Table A-3 Acceleration Factor Calculations

Parameter	ALT I	ALT II
f (cycles per day)	36	36
T(°C)	160	140
T _{max} (K)	433	413
Acceleration Factor	155.50	105.87
N _{test} (cycles)	225	330

Quantification of Functional Failure Probability of a Passive Safety System

Chandrakar A.¹, Nayak A. K.², Vinod Gopika³

¹Homi Bhabha National Institute, Anushaktinagar, Mumbai

²Reactor Engineering Division, Reactor Design Development Group, Bhabha Atomic Research Centre, Mumbai

³Reactor Safety Division, Reactor Design Development Group, Bhabha Atomic Research Centre, Trombay, Mumbai
Email: amityy2002@gmail.com

Abstract

In nuclear power plants there are many process control systems and safety systems that work together simultaneously. Many of the advanced reactors are designed to utilize passive safety systems, which do not have any moving mechanical components; however most of the passive systems use valves for either activation or during the operation. Static reliability analysis techniques such as event tree and fault tree analysis, assume that such valves have binary-states of failure (stuck open and stuck closed). However, these valves can fail at intermediate positions of opening as well. These partial failures of components can have dominant effect on the reliability of passive systems. Most of the failure databases, report binary-state failure probability of valves and do not provide any information about the intermediate state failure probabilities. In this paper, we conducted experiments and evaluated the probability of such valves failing at partial openings. These probabilities were determined on a dynamic reliability benchmark setup of holdup tank having three control valves and their associated control mechanisms. It was found that the probability of failure at intermediate states is considerably high and cannot be ignored for analysing the passive systems reliability. The importance of considering intermediate state failure probabilities of such components in passive system reliability analysis, is presented by analyzing the reliability of a passive isolation condenser system of an advanced reactor as an example.

Keywords: Multi-state failure; Passive systems; Control valves; Advanced reactor.

1. Introduction

In nuclear power plants, there are many process control systems and safety systems which work together. Many of the advanced reactors are designed to utilize passive safety systems, which do not have any moving mechanical components [1]; however most of the passive systems use valves for either their activation or during the operation of these systems. For example, in passive decay heat removal system of advanced reactors, isolation condensers are used. The passive operation of heat removal is activated by opening of passive valves and a process control valve. These valves open and closes based on the signals of some process parameters like steam drum pressure, etc. The opening and closing of these valves is accomplished by electrical, hydraulic or pneumatic actuators, which get control signals from proportional

integral differential (PID) controllers. Static reliability analysis techniques such as event tree and fault tree analysis, assume that such valves have binary-states of failure (stuck open and stuck closed). However, such components can fail at intermediate positions as well. For example, a control valve can fail at 10% stuck open or 25% stuck open or at any other percentage of openings. In addition, it is also possible that the fault may increase/decrease in a particular direction with respect to time. These dynamic failure characteristics are often ignored in the static reliability analysis. Besides this, there can be certain other dynamic characteristics which may influence the reliability estimates of system. Most of the failure databases like IAEA [2]; NSWC [3] and MIL-HDBK-217E [4], report binary-state failure probability of valves, and do not provide any information about the intermediate state failure probabilities.

In this paper, we conducted experiments and evaluated the probability of such valves failing at partial openings. These probabilities were determined on a dynamic reliability benchmark setup of holdup tank having three control valves and their associated control mechanisms. It was found that the probability of failure at intermediate states is considerably high and cannot be ignored for analysing the passive systems. The importance of considering state failure probabilities of such components in passive system reliability analysis is presented by analyzing a passive isolation condenser system of an advanced reactor as an example.

The article is organised as follows. The methodology for determining the intermediate state failure probabilities of valves is presented in section 2. In section 3, the reliability analysis of passive isolation condenser system of an advanced reactor considering the partial failure probabilities of valves is presented. The article is then concluded in section 4.

2. Methodology for Determining Functional Failure Probabilities of Valves at Multiple States of Opening

In order to determine the probability of valves failure in intermediate positions of opening during operation of passive system, an experimental setup of hold-up tank was utilized. The details of the setup are discussed below:

2.1. Experimental Set-Up

The experimental set-up consists of a fluid containing tank, which has three separate level control units. Fig. 1 shows a simplified line diagram of the set-up and Fig. 2 shows the actual photograph of the experimental set-up. Each control unit is independent of the other and has a separate level sensor associated with it. The level sensors measure fluid level in the tank, which is a continuous process variable. Based on the information from level sensors, the operational state of the control units is determined. Each flow control unit can be thought of as containing a controller which turns the unit "on" and "off" based on the signal from the level sensors, as shown in Fig. 2. Failure of the system occurs when the tank either runs "dry" or "overflows".

Total length of the tank in the experimental setup is 1 meter. The tank has a nominal fluid level at the start of system operation. This nominal level is assumed as zero meters for the simulation which corresponds to 0.5 meters in the experimental set-up;

all levels are measured with reference to this zero level. The level which are above zero are referred as positive whereas below ones are negative. The maximum level of the tank for experimental considerations is +0.4 meter and the minimum is -0.4 meter. If the tank level moves out of this range, failure of the system will occur. Within this range, there are two set points at -0.2 meter and +0.2 meter. These set points define three control regions for system operation. Region 1 is defined from point -0.4 meter to -0.2 meter; region 2 is from -0.2 meter to +0.2 meter; and region 3 is from +0.2 meter to +0.4 meter. When the fluid level is in any of the three control regions, there is a specific action required for each of the three control units. During normal operation, the level is in region 2 (i.e. in between -0.2 meter and +0.2 meter). In this region, unit 1 and 2 are in ON position so the flow is coming from unit 2 and outgoing from unit 1. Due to any failure or transient when level starts falling and reaches region 1 (i.e. in between -0.2 meter and -0.4 meter), the system goes into a transition of state by turning OFF the unit 1 and switching ON the unit 3 and unit 2 so that the level in the tank rises to reach normal operating region 2. Similarly, when the level in the tank reaches upper control region 3 (in between +0.2 meter and +0.4 meter), the system goes into transition of state by switching unit 2 and 3 OFF while keeping unit 1 in ON position so that level can drop to normal operating range (region 2). Overflow failure occurs when level exceeds +0.4 meter mark and dryout happens when it dips below -0.4 meter mark.

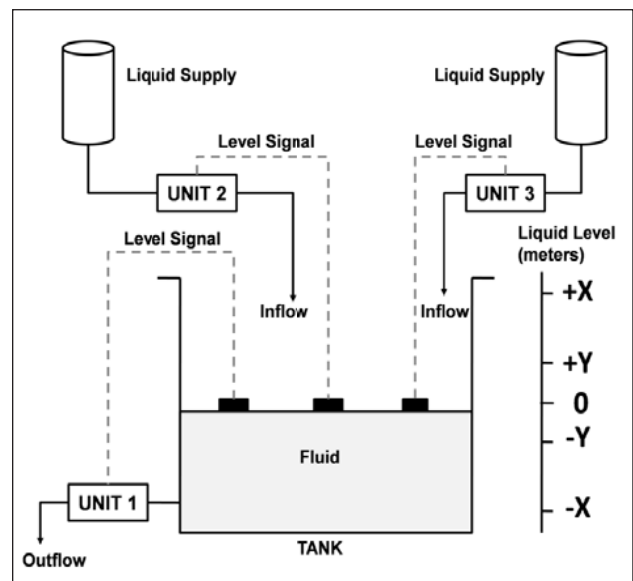


Fig. 1 Simplified schematic of experimental set-up

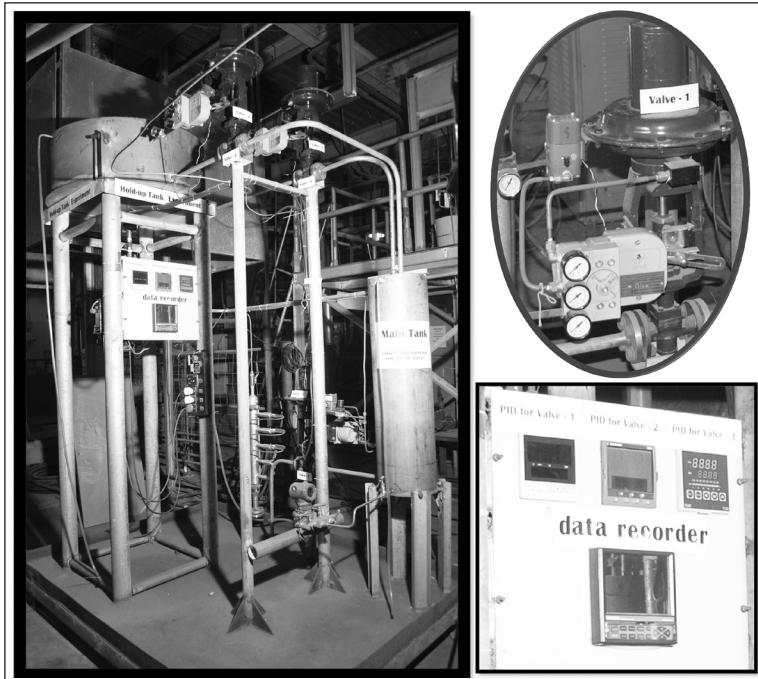


Fig. 2 Experimental set-up

2.2 Methodology in Steps

In order to simulate the actual failure of valves, the valves were made to fail in the experiment by disabling the control of that particular valve. Once the fault in the valve is initiated, it can get stuck at any positions of operation. However, the stuck position of operation cannot be read by using the PID controller, because they were disabled to simulate the failure of valve. In order to get the failed position of valve, the experiment was continued to record the actual failure of system i.e. either overflow or dryout. Once the time to failure of the system was recorder from the experiment, many configurations (% of stuck conditions) of the faulty valve were simulated using the methodology presented by Chandrakar et al.[5]. From the output of the simulation, the fault position was selected by comparing the system failure time obtained from the experiment and simulation. The above mentioned procedure was repeated for a large number of configurations and combinations of valve. The result so obtained are analysed and a histogram of fault positions is plotted to get the probability of failure at intermediate states of operations of each valve. The above mentioned procedure is delineated in steps with one example illustrated below:

Step 1: Initiation of Fault

In the experimental setup, the fault is induced in valves by disabling the automatic controller (PID). This fault is induced at the start of the operation

when the main tank is at nominal operating condition.

Observation: The fault in valve 1 was induced. Once the fault in the valve is initiated, it can get stuck at any positions of operation.

Step 2: Record the System Failure Time

Continue the experiment to record the system failure. Failure of the system can be overflow or dryout based on the system dynamics and state of the valve failure.

Observation: System fails in overflow and time to failure was 653 minutes.

Step 3: Estimate the Fault Position

Simulate many configurations (% of stuck conditions) of the faulty valve using the methodology presented by Chandrakar et al. [5]. From the output of the simulation, select the fault position by

comparing the system failure time obtained from the experiment and simulation.

Observation: A number of different cases with different fault positions were simulated using the methodology presented in Chandrakar et al. [5]. Table 1 presents the simulated cases. From the output of the simulation, the fault position of 75% stuck was selected by comparing the system failure time obtained from the experiment and simulation.

Table 1: Simulated Cases of Fault in Valve 1

V1	V2	V3	Failure type	Failure time
100%	100%	100%	No failure	NA
75%	100%	100%	Overflow	652.9
50%	100%	100%	Overflow	301.3
25%	100%	100%	Overflow	221.1
0%	100%	100%	Overflow	156.2

Step 4: Repeat Step 1-3

Steps 1-3, are repeated for a possibly large number of times. Accuracy of estimates of state probabilities increases by increasing the number of times the experiments are repeated. However, the constraints on the time and resources often put restrictions on this.

Total of 100 experiments were performed as per the steps mentioned in section 2.2. The result so obtained from the experiments and simulations were analysed and a histogram of fault positions was plotted (Fig. 3)

to get the probability of failure at intermediate states of operations of valves (Table 2).

Table 2: Probability of Valve Failure at Intermediate States

% Fault	Probability of getting stuck
Stuck close - 100%	≈35%
Stuck intermediate-25%	≈5%
Stuck intermediate-50%	≈10%
Stuck intermediate-75%	≈15%
Stuck open - 100%	≈35%

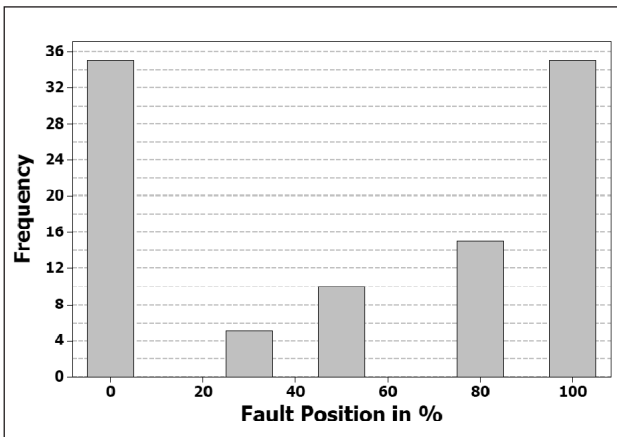


Fig. 3 Histogram of fault positions obtained from 100 experiments

3. Application of Partial Failures of Valves in Passive System Reliability Assessment

Importance of considering partial failures of components like valves can be better understood by analyzing and estimating the function failure probability of a passive safety system considering the probabilities of valve failure as presented in Table 2. For this purpose a passive isolation condenser system of an advanced reactor is considered.

3.1 System Description

The Indian Advanced Heavy Water Reactor (AHWR) is a 300MWe (920MWth) pressure-tube type boiling- water reactor employing many passive features. Natural circulation as the desired heat removal mode from the core under all conditions of operation is the most important passive concept adopted in this reactor. Decay heat removal is also accomplished in a passive manner by establishing a natural circulation path between the Main Heat Transport System (MHTS) and the Isolation Condenser System. Fig. 4 shows the general arrangement of MHTS and ICS of AHWR. The main heat transport system

consists of a vertical core having coolant channels (452 nos.) arranged in a calendria. The two- phase mixture leaving the coolant channels is carried to the steam drum (4 nos.) through corresponding tailpipes (risers). Steam drum is a horizontal cylindrical vessel with appropriate internals, where gravity separation of two-phase mixture is achieved. Nearly dry saturated steam leaves the steam drum through steam lines to feed the turbines. Recirculation water is mixed with feed water in the steam drum and it flows through the downcomer (4 nos. per steam drum) which are connected to a header which in turn is connected to coolant channels through corresponding feeders.

Isolation Condenser System comprises of a set of immersed condensers located in an elevated water pool called gravity-driven water pool (GDWP), and associated piping and valves. A branch connection from the steam line carries the steam to tube bundle of immersed condenser through a distributor and top header. The steam condensation takes place in the tube bundle and the condensate returns to the downcomer region of steam drum through a bottom header and condensate return line. The condensate return line is provided with a set of active and passive valves in parallel. The heat removal capacity is regulated using a passive valve where the valve opening is regulated passively depending on steam drum pressure thus maintaining hot shutdown. Hot shutdown state refers to the condition of zero reactor power (core under decay heat) with the steam drum pressure in range of 76.5–79.5 bar (with corresponding saturation temperature) such that reactor can be started and powered after short duration outage. This is different from the cold shutdown state wherein the reactor coolant is cooled down to atmospheric pressure and temperature of about 40 degree Celsius. The passive valve is a self-acting single-port spring-loaded valve with pressure balancing by stainless steel bellows, working in proportional mode requiring no external energy-like pneumatic or electric supply for its actuation. The valve uses the steam drum pressure as the signal and has the linear characteristic, i.e. valve opening varies from fully closed to fully open with the variation of steam drum pressure in the specified range. The active valve (pneumatically operated) provided in parallel serves the purpose of bringing system to cold shutdown condition, if required. Under normal operation, valves remain closed thus isolating the ICS from the MHTS, and steam flows to the turbine circuit. Whereas, under shutdown conditions, turbine gets isolated from the MHTS, passive valve opens (and

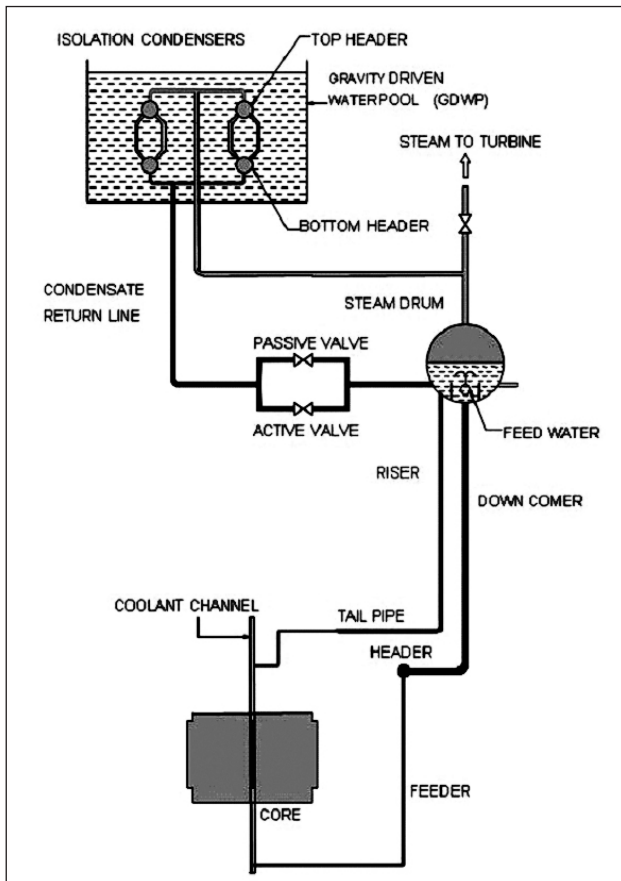


Fig. 4 Schematic MHTS and ICS of AHWR

closes also) in response to steam drum pressure and a natural circulation path gets established between MHTS and ICS.

3.2 Reliability Analysis of Isolation Condenser System in Steps

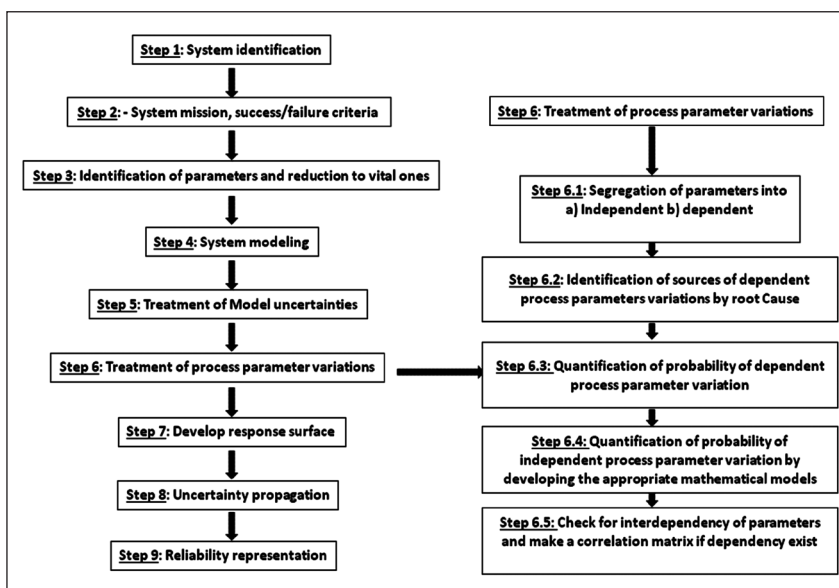


Fig. 5 The APSRA+ methodology

The reliability of an isolation condenser system has been analysed using APSRA+ methodology. APSRA+ methodology is presented in Fig. 5. The stepwise methodology to evaluate reliability of this system is described as follows

Step 1: System Identification

In step 1, the passive system for which reliability will be evaluated is considered. The system being considered is the Isolation Condenser System (ICS) of Advanced Heavy Water Reactor (AHWR).

Step 2: System Mission, Success/Failure Criteria

System Mission: mission of the isolation condenser system is to provide a heat sink which would condense the steam generated by the stored heat, fuel decay heat and will limit the pressure rise in the steam drum and prevent the clad temperature under threshold for grace period of 3 days without operator intervention.

Failure Criteria: ICS is coupled to MHTS, any set of conditions that lead to excess peak clad temperature above 400°C is ascribed to failure of ICS. Thus, ICS is considered to be failing if it fails to maintain the peak clad temperature under 400°C for the duration of 3 days.

Step 3: Identification of Parameters

Parameters that were identified in this step include:

- a. presence of non-condensables in IC;
- b. water level in gravity driven water pool (GDWP);
- c. GDWP water temperature;
- d. active valve availability;
- e. passive valve availability;

Step 4: System Modeling

The performance of ICS coupled with MHTS was modeled using RELAP5/Mod 3.2.

Performance under Normal Operating Range of Process Parameters

Isolation condenser along with main heat transport system is analyzed for the normal condition of operation as a base case. This

normal operating condition of ICs corresponds to 0% non-condensable, 100% submergence of IC tubes in GDWP water and 40°C normal operating temperature of GDWP water. Performance under normal condition is depicted in Fig. 6. With initiation of station blackout (SBO), decay heat is continuously added to the fluid. The main condenser including feed water is unavailable at t=1500 s. The main heat transport system is boxed. As a consequence of this, steam drum pressure increases from normal operating to 7.65MPa over the period of 700 s. At this pressure, passive valve begins to open and thereafter pressure is maintained by regulating passive valve opening area as shown in Fig. 6(b). Core decay power and heat rejection in IC are closely matching, and, in turn maintaining the SD pressure constant. Under this condition, active valve remains closed, as it opens only when steam drum pressure reaches 80 bar or after 30 minutes of operation of Isolation condenser, However, for understanding the effect of dynamism involved in the operation of valves and their effect on the passive system operation, active valve is restricted to open only when SD pressure rises beyond 80 bar. As shown in Fig. 6(c), clad temperature remains constant and under the threshold.

Performance Under Degraded Conditions

In order to determine the effect of the parameters identified in Step 2 on system performance, sensitivity

analysis of the various parameters is performed using RELAP5/Mod 3.2. The parameters are varied over a range as given in Table 3 and their effects on system performance are described in the following sections.

Table 3: Parameters Affecting System Performance

SI. No.	Parameter	Normal operating condition	Range of variation
1.	Non condensables in IC circuit	0%	0-100%
2.	GDWP water temperature	40°C	30-90°C
3.	Water level in GDWP	9 m	0-9 m
4.	Active valve availability	100%	0-100%
5.	Passive valve availability	100%	0-100%

Active and Passive valve availability: The passive and active valves in isolation condenser can fail at any intermediate positions other than stuck open or stuck closed. In order to understand the system behavior when active and passive valves fail at intermediate positions of opening, valve failures were simulated using RELAP5/mod3.2. Let us look at the effects of simultaneous failure of active and passive valves. It was observed in simulations that clad temperature rises above 400°C only when both valves fail during

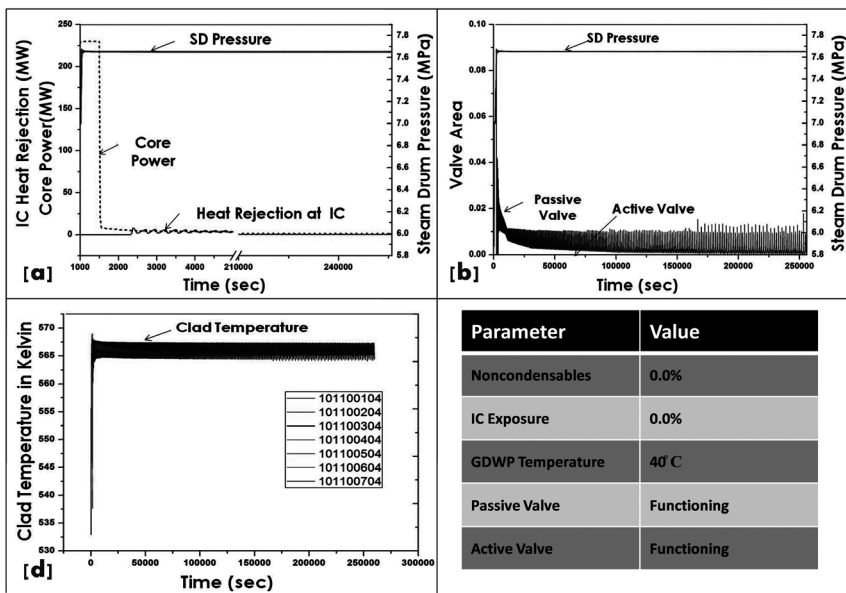


Fig. 6 (a) Variation of SD pressure, core decay power and heat rejection through IC with time during SBO transient in absence of degrading factors, (b) Passive and active valve opening area during the operation of IC, (c) Clad temperature during the operation of IC

the assumed SBO transient. When all the other parameters are in nominal range, it was observed that when the active and passive valves fail in less or equal to 0.1% of opening, the clad temperatures rises beyond 400°C. However, beyond 0.1% of opening, the clad temperature has the tendency to fall, since the mass flow across these valves are sufficient enough to cool the reactor dissipating the decay heat. It was also noted that when all the parameters (%NC, GDWP temp and %IC exposed because of GDWP level drop) are in nominal range, the system can fail only when passive valve fails first following which, active valve is triggered and subsequently fails on demand.

However, in case of parameters exceeding the limiting values, since both the passive and active valves are called on demand, the sequence of failure does not matter. Various failure cases obtained by individual and combined variations of the parameters are discussed below.

Effect of non-condensables: For the purpose of this analysis, non-condensables (NC) are assumed to be initially present in the system. Steam drum to IC line is filled with steam-air mixture of a different concentration as an initial condition. GDWP water is at nominal and IC tubes are fully submerged in water. The assumed transient is initiated. At NC mass fraction of 6.5%, IC is found to fail to maintain hot shutdown, as shown in Fig. 7(a). At this NC fraction, it is found that though the passive valve is fully open, it is not able to maintain the SD pressure, due to degraded condition of heat transfer resulting in poor condensation of steam, causing the pressure to rise. As the pressure reaches 80 bar, active valve opens. With opening of active valve, SD pressure reduces to 76.5 bar that leads to closing of passive valve, but pressure continues to

drop as active valve continues to remain open. Under such conditions, system inadvertently undergoes cold shutdown. During this scenario of NC mass fraction of 6.5%, if passive and active valve fails stuck (total passive+active opening area <0.2%) on demand, the clad temperature rises beyond 400° C within 3 days of grace period as depicted in Fig 7(b).

Effect of GDWP water temperature: With the simulation results, it was observed that, even at GDWP water temperature 90°C; the system is maintained under hot shutdown. Under this condition it was found that heat transfer condition has rather improved due to local boiling in the pool near the top node of IC tubes. A typical case of failure (i.e. clad temperature exceeding 400°C) at GDWP temperature of 50°C and 5.5% NC, is observed in case of passive and active valve fails stuck closed partially (total <0.2% of their opening area) during SBO.

Effect of GDWP water level: As an initial condition, the steam drum to IC line is filled with pure steam and GDWP water temperature is at 40°C. IC tubes external surface is partially exposed by reducing GDWP water level. The hot shutdown is successfully maintained with 75% exposed IC tubes. This may be attributed to huge coolant inventory available in the pool. A typical case of failure due to exposure of IC tubes is observed at 87.5% exposed of IC tubes. At this condition, if the passive and active valve fails in stuck closed condition partially (total <0.2% of their opening area), the clad temperature rises above 400°C.

Combined effect of NC, GDWP water level and temperature: Based on the effect of degrading factors individually various combinations are considered. A typical failure case of 62.5% exposed tubes with 4.2% NC and 90°Celsius pool water temperature when active and passive valve fails stuck partially (total <0.2% of their opening area).

Step 5: Treatment of Model Uncertainty

In absence of adequate operational experience with passive systems, it is customary to depend on the prediction of their performance by best estimate codes. The applicability of best estimate codes such as RELAP5/Mod 3.2 to model such systems and capture various phenomena associated with such systems is questionable as the currently available best estimate codes were developed mainly for active systems. As a consequence of this, prediction of passive system performance is associated with uncertainties which can significantly influence the prediction of natural circulation characteristics and hence its reliability.

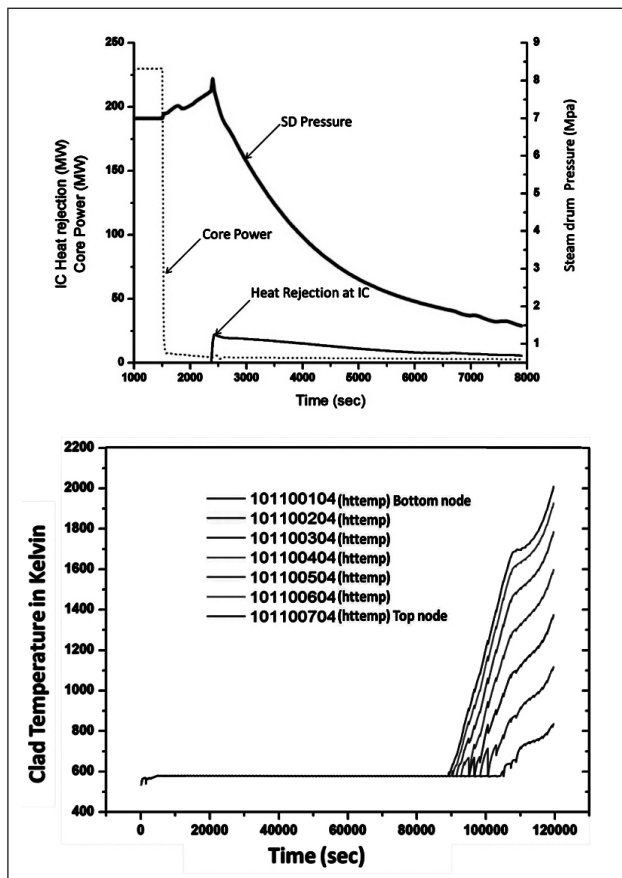


Fig. 7(a) Variation of SD Press, Core power and Heat rejected at IC in Presence of 6.5% NC; (b) Clad temperature in Presence of 6.5% NC with active and passive valve failed stuck closed <0.2%

Model uncertainties considered for this analysis are: (1) Heat Transfer Coefficient (HTC), (2) Pressure Drop (ΔP), (3) Choking Flow (c), (4) Abrupt Area Change (a), (5) CCFL (f), and (6) Modified Energy Term (e). On the basis of analysis of various combinations of the degrading factors, various failure points have been achieved.

Step 6- Treatment of Process Parameter Variations

Treatment of process parameter variations is performed in several steps:

Step 6.1: Segregation of Parameters Into

a) Dependent Parameters

b) Independent Parameters

Process parameters are segregated as follows:

Dependent Parameters: Non condensables, GDWP Temperature, GDWP level and passive and active valve availability

Independent Parameters: None

Step 6.2: Identification of Sources of Dependent Process Parameters Variation by Root Cause

- a) Non-condensables: A close examination to the system reveals that control valves were used in the purging/ venting system of non-condensables. The accumulation of non-condensable can be attributed to the failure of these control valves to remain open during the normal operation of reactor.
- b) GDWP Level: The root cause for this parameter reveals that the cause for this parameter variation is failure of makeup circuit.
- c) Active and Passive valve availability: Valve failure in itself is a hardware failure, hence no further root cause was performed. However, the valve failure can be further explored to the basic cause and its mechanism of failure by using physics of failure models.
- d) GDWP Temperature: The primary cause of high temperature of GDWP water is the failure of GDWP recirculation system.

Step 6.3: Quantification of Probability of Dependent Process Parameter Variations

- a) **Non Condensables:** Accumulation of non-condensable is attributed to the failure of the purging/vent valves to remain open during

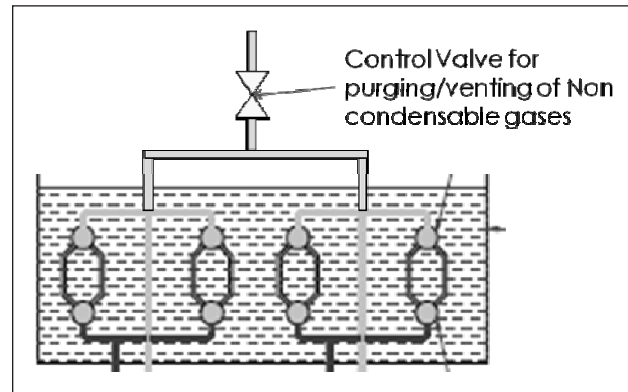


Fig.8 Schematic of purging/vent system for one set of isolation condensers

the normal operation of reactor. A simplified schematic of the venting valves for one set of isolation condenser is presented in the Fig. 8.

To quantify the probability of presence of non-condensable during the startup of isolation condenser operation, the following assumptions were made:

- The inspection time for the purging/vent control valves is considered to be 48 hrs.
- A typical undetected failure in between test inspections is considered to be half of the inspection time. In this case it would be 12 hrs.
- In actual reactor, for quarter core (1/4th total power) the non-condensable accumulation over a 3 hrs period will be 6.2 kg (~ 1% of non-condensable as per our basis of calculation).
- Valve stuck probabilities considered in this analysis are per Table 2

With the above mentioned assumptions, the mathematical relation between non condensable generation rate can be expressed by eq.1.

$$\text{NC generated in \%} = \text{NC generated per hour} * \text{No of hours spent after valve failure} \text{---(1)}$$

The methodology of dynamic reliability mentioned in [5] was adopted to get the estimate of frequency of non condensable gases. The flow diagram of the methodology adopted for this case is presented in Fig 9.

Non-condensable gas present during the startup of the operation of isolation condenser system,

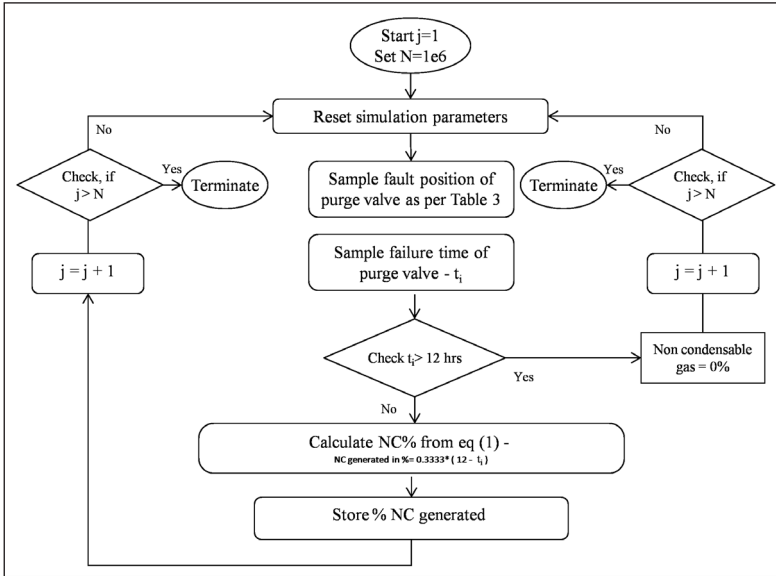


Fig.9 Flow chart of the methodology for deriving the probability of non-condensable% present during the startup of ICS

it causes the non-condensable gases to accumulate. However, in actual the valve can fail in intermediate positions as well, and the partial failure will not always lead to very high non-condensable gas accumulation. These two factors: a) partial failure of purging valve b) time accumulated after the valve failure; were considered to estimate the presence of non-condensables probability. When these factors were considered, the probability of non-condensables present during the startup of the ICS was estimated to be very less than the one considered in binary failure case.

b) **GDWP Level:** The GDWP level fall causes IC tubes to be exposed to the atmosphere. The effect of GDWP level can be directly represented

based on this analysis is shown in Fig. 10. It is to be noted that the probability of non-condensables present in the ICS was considered as a constant (Probability of high NC=1e-4)[14] in case when only binary failure states was considered. However, considering the multi-state failure of valves leads to the probability values to be varying with respect to the percentage of non-condensable present during the start of the operation. The probability values are conservative in static analysis (binary failure cases) when compared to the multi-state failure considered case. In static analysis, the probability of presence of non-condensable gases is attributed to the failure of the purging valve. It was assumed that this valve fails in binary mode (i.e stuck closed or suck open) and whenever the valve fails in stuck closed mode,

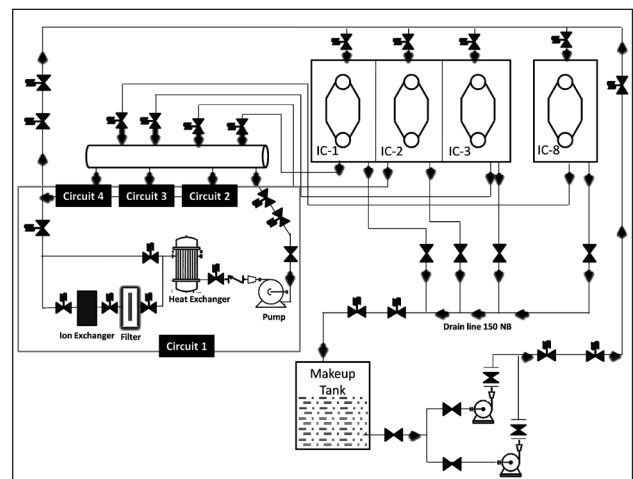


Fig. 11 GDWP makeup and recirculation schematic

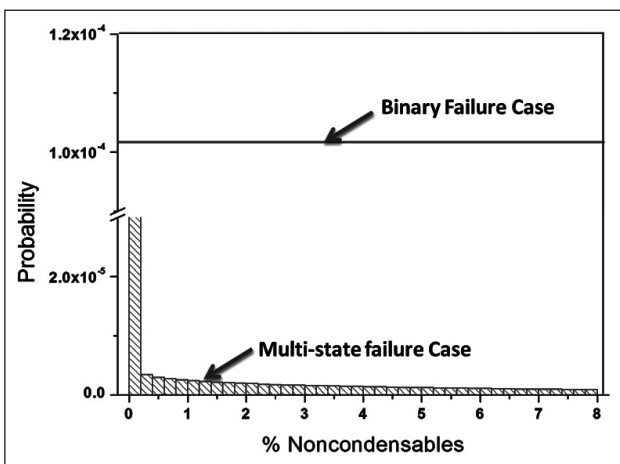


Fig.10 Probability of non-condensable present at the startup of ICS operation

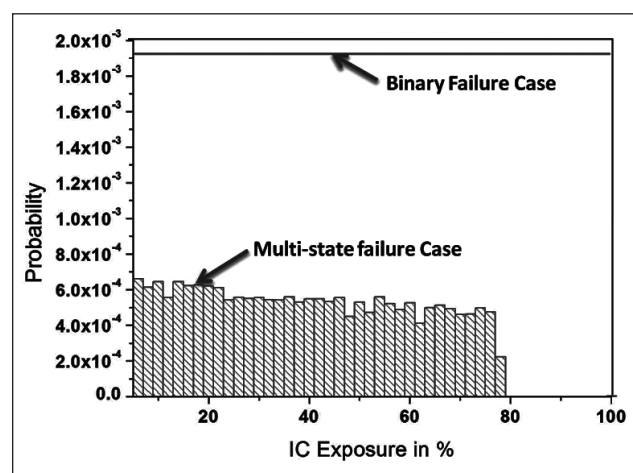


Fig.12 Probability of percentage of IC exposure

by IC exposed. Hence the effect is represented by the %IC exposed. Since the GDWP level can fall primarily because of the failure of the makeup circuit, which consists of many valves (schematic presented in Fig. 11), a simulation similar to non-condensable gas probability estimation was adopted with appropriate modifications to model the behavior of these valve failures. The simulation result is shown in the Fig. 12.

c) **GDWP Water Temperature:** The GDWP water temperature is maintained by the heat

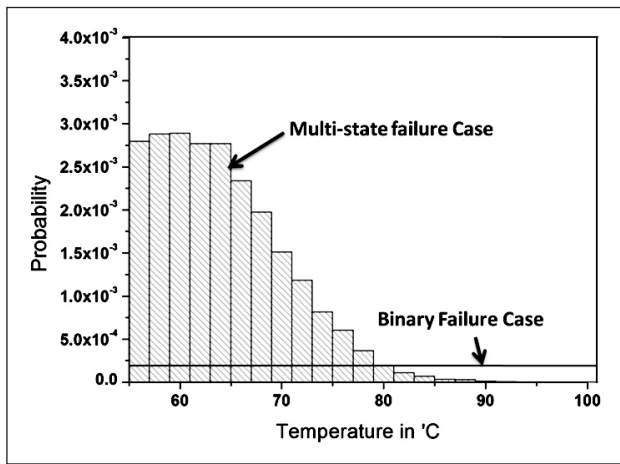


Fig.13 Probability of high GDWP temperature

dissipation in the recirculation loop. Hence the GDWP water temperature rise is attributed to the failure of recirculation loop, which consists of many valves (schematic presented in Fig. 11), a simulation similar to non-condensable gas frequency generation was adopted with appropriate modifications to model the behavior of these valve failures. The simulation result is shown in the Fig. 13.

Step 7: Generation of Response Surface of Failure Causing Parameters

Response surface of limiting surface for cases a) without model uncertainties and b) with model uncertainties was developed (Fig.14). In both the cases the limiting value of non-condensable was considered as response and % IC exposed and GDWP temperature were considered as input variables. For estimating the probability of parameters falling outside the limiting surface, all three parameter values were generated for 1E+07 number of Monte Carlo runs based on their mathematical models or pdf developed. The limiting value of non-condensables were calculated from the response surface equation using % IC exposed and

GDWP temperature as inputs. The sampled non-condensable values were then compared with the limiting value of the non-condensable calculated from response surface equation. If sampled value of non-condensable was found more than the limiting value, this indicated that point lies beyond the limiting surface.

Response surface for case a) without considering model uncertainties: A full quadratic model was used to model the response surface. The fitted model has R² – 88.7% and R²-adjusted -84.0%, which ensures that the fitted model is good approximation of the response surface. The equation for response surface without considering model uncertainties is given by eq. (2):

$$\% \text{ NC} = 6.52468 - 0.00207 * \% \text{ IC_exposed} - 0.01407 * \text{gdwp_temp} - 0.00058 * \% \text{ IC_exposed}^2 - 0.00003 * \text{gdwp_temp}^2 + 0.00017 * \% \text{ IC_exposed} * \text{gdwp_temp} \text{ -----(2)}$$

Response surface for case b) with considering model uncertainties: A full quadratic model was used to model the response surface. The fitted model has

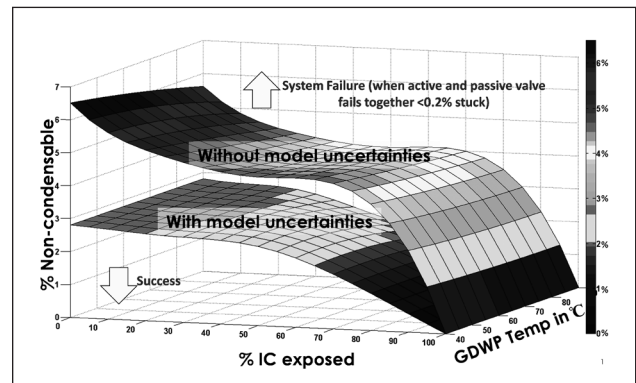


Fig. 14 Failure surface with and without considering model uncertainties

R² – 98.3% and R²-adjusted -97.7%, which ensures that the fitted model is good approximation of the response surface. The equation for response surface with considering model uncertainties is given by eq. (3):

$$\% \text{ NC} = 2.32193 + 0.00787 * \% \text{ IC_exposed} + 0.01637 * \text{gdwp_temp} - 0.00032 * \% \text{ IC_exposed}^2 - 0.00014 * \text{gdwp_temp}^2 - 0.00005 * \% \text{ IC_exposed} * \text{gdwp_temp} \text{ -----(3)}$$

Step 8: Uncertainty Propagation:

From the analysis of isolation condenser system, it was found that clad temperature exceeds the threshold value of 400°C in the events when process parameters affecting the performance lie on or outside the failure surface and both passive and active valves fail.

Probability of any parameters falling outside the failure surface was estimated by using a Monte Carlo simulation. For the Monte Carlo simulation process parameter values were sampled based on the probabilities estimated in step 6. Each generated sample combination of process parameters were checked to find if it lays above or below the failure surface. Combination of valve failure probability was also estimated using Monte Carlo simulation. Finally the probability of IC fail to maintain the clad temperature below 400°C was estimated by multiplying the failure probabilities of valves and process parameters exceeding the failure surface.

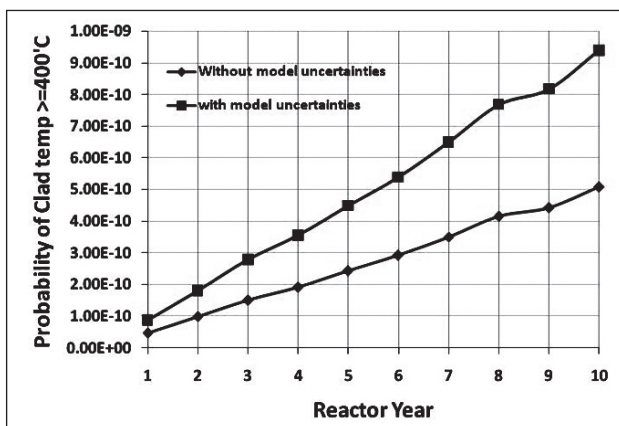


Fig. 15 Probability of failure of ICS with respect to the reactor years

Step 9: Reliability Representation with Uncertainty Bounds Of Model Errors

Probability of ICS failure is presented in Fig.15. Probability of failure with considering the model uncertainties can be treated as confidence bounds on probability of failure. It can be seen that the probability of failure considering model uncertainties is higher than without considering the model uncertainties for isolation condenser system.

4. Conclusions

In nuclear power plants, there are many process control systems and safety systems which work together. Many of the advanced reactors are designed

to utilize passive safety systems, which do not have any moving mechanical components; however most of the passive systems use valves for either activation or during the operation of these systems. Static reliability analysis techniques such as event tree and fault tree analysis, assume that such valves have binary-states of failure (stuck open and stuck closed). However, such components can fail at intermediate positions of opening as well. Most of the failure databases, report binary-state failure probability of valves and do not provide any information about the intermediate state failure probabilities.

In this paper, we conducted experiments and evaluated the probability of such valves failing at partial openings. These probabilities were determined on a dynamic reliability benchmark setup of holdup tank having three control valves and their associated control mechanisms. It was found that the probability of failure at intermediate states is considerably high and cannot be ignored for analysing the passive systems reliability. The importance of considering state failure probabilities of such components in passive system reliability analysis is presented by analyzing the reliability of a passive isolation condenser system of an advanced reactor. From this study, it can be concluded that quantification of functional failure probability of passive system is very much dependent upon the characteristics and probability of failure of its vital components like valves.

References

1. Nayak A.K., Chandrakar A., Vinod G. A review: passive system reliability analysis –accomplishments and unresolved issues. *Frontiers Energy Research* 2014; 2:40. DOI: 10.3389/fenrg.2014.00040
2. International Atomic Energy Agency. (1988). *Component Reliability Data for Use in Probabilistic Safety Assessment*. Vienna: IAEA.
3. NSWC. (2006). *Handbook of Reliability Prediction Procedures for Mechanical Equipment*.
4. MIL-HDBK-217E. (1986). *Reliability Prediction of Electronic Equipment*. Rome: Air Development Center.
5. Chandrakar, A., Nayak, A. K., and Gopika, V. (2014). Reliability analysis of process controlled systems considering dynamic failure of components. *Int. J. Syst. Assur. Eng. Management*; 6(2): 93-102. doi:10.1007/s13198-014-0248-z.

Numerical Solution of Shielding Integrals Using Monte Carlo Simulation Method

Avijit Das, Tej Singh and P. V. Varde

Research Reactor Services Division, Reactor Group, Bhabha Atomic Research Centre, Mumbai – 400085
Email: t_singh@barc.gov.in

Abstract

Integrals appeared in shielding analysis for extended source shield geometry are difficult to evaluate by using first principle due to the implicit form of the parameters such as attenuation coefficient, material thickness, energy, geometrical dimension, etc. Monte Carlo simulation being a numerical and statistical enriched method of evaluation of integration, this paper aims an application of this Monte Carlo technique to evaluate the shielding integrals. Paper presents the details of the scheme of this evaluation with proper example. Evaluation of the integral appeared in shielding formulation of a self absorbing cylindrical volume source as well as spherical volume source along with rectangular shield geometry is presented in this paper. Numerical stability of these integrals are also discussed.

Keywords: Monte Carlo, Shielding, Extended source, attenuation coefficient

1.0 Introduction

Computation of the shielding thickness of a specific material such as concrete, lead or iron for gamma photons on the basis of point kernel technique has already been practiced for decades. Point kernel based shielding code for gamma photons are available in many literatures [1-4]. Radiation protection communities provide the support of adequacy checking of shielding thickness for any nuclear facility that handles radioactive sources. Even though computer codes for shielding analysis are well validated, it is very much desire to have always some fast calculation of the shielding thickness as ready reckoned; especially during operation of the facility. Standard practice in this regard is always fruitful because user will know the analytical expression of the photon flux in presence of a shielding of specified thickness and then just by multiplying photon flux to dose conversion factor, dose rate at the target point can be easily obtained. However, it is a very true fact that integrals appeared in the expression of photon flux for an extended source-target shielding geometry [5-6] are not analytically solvable. Researchers approach available in literatures so far is based on tabular values or monographs [7-8]. But these analytical tools very often fail to provide the true estimate of these integrals. In order to improve this difficulty while evaluating the integrals for computing gamma dose rate, Monte Carlo Integration technique (MCI) has been applied. MCI is a

powerful method for computing the value of complex integrals using probabilistic techniques. It should be noted that MC based approach of shielding analysis is completely different from the present approach of usage of MC in the shielding problem. In Monte Carlo simulations of shielding problems, the code tracks the fates of individual photons as they move through the shield [9-12]; decisions as to how far a photon travels before interacting, what type of interaction occurs, what direction is taken by scattered photons, etc., are all made on a probabilistic basis in which random numbers are selected and associated with specific probabilities that are used to specify the decision outcome. Thus, if the fates of two identical photons are followed, we would expect them to be different much of the time, and it is only by investigating enough photons that we might expect the overall results to be representative of reality-e.g., that the determined dose at a receptor location will be correct. Two individuals running the same Monte Carlo code to solve the same problem will not necessarily arrive at exactly the same answers. This paper will only address the evaluation of the complex integrals appeared in radiation shielding by using MC technique. Technique will be demonstrated with the help of a problem on gamma photon flux at any target point due to a self-absorbing cylindrical volume source in presence of shield. Remaining part of the paper has been organized in this way: section 2.0 will describe the mathematical background of Monte Carlo Integration. Section 3.0

presents the actual problem for demonstration. Section 4.0 presents the results and discussion.

2.0 Mathematical Background of Monte Carlo Integration

Monte Carlo Integration [13-14] is a simple and powerful technique for approximating complicated integrals. Assume we are trying to estimate the integral of a function f over some domain D :

$$F = \int_D f(\vec{x}) d\mu(\vec{x}) \tag{1}$$

Once again, vector notation is used to indicate that f need not be one-dimensional. In fact, Monte Carlo techniques are used mostly for higher-dimensional integrals, or integrals that cannot be evaluated analytically. Assume that we have a PDF p defined over a domain D . Then the above integral is equivalent to

$$F = \int_D \frac{f(\vec{x})}{p(\vec{x})} p(\vec{x}) d\mu(\vec{x}) \tag{2}$$

The expected value of

$$\frac{f(\vec{x})}{p(\vec{x})} \tag{3}$$

with respect to a random variable distributed according to $p(\vec{x})$.

It is also possible to estimate the value of the expectation of $f(x)/p(x)$ by generating a number of random samples according to p , computing f/p for each sample and finding the average of these values. As more and more samples are taken, this average is guaranteed to converge the expected value, which is also the value of the integral. This process of averaging the value of $f(x)/p(x)$ for multiple random samples to estimate the value of an interval is called Monte Carlo Integration.

Suppose we have a circle inscribed within a square. Let N be the number of darts thrown towards the circle with an objective that they should be within the circle and n^* be the number of darts that land inside the circle. If A is the area of the square, the area of the circle is

$$I = \frac{n^*}{N} A \tag{4}$$

Thus, the circle's area is approximately equal to the area of the square multiplied by the fraction of

darts that landed inside the circle. One can apply this simple idea.

Suppose it is required to evaluate the integral

$$I = \int_R f(X) dX \tag{5}$$

where R is an n -dimensional space. Let $X = (X^1, X^2, \dots, X^n)$ be a random variable that is uniformly distributed in R . Then, $f(X)$ is a random variable whose mean value is given by

$$\overline{f(X)} = \frac{1}{|R|} \int_R f(X) dX \tag{6}$$

and the variance by

$$\text{var}(f(X)) = \frac{1}{|R|} \int_R f^2(X) dX - \left(\frac{1}{|R|} \int_R f(X) dX \right)^2 \tag{7}$$

where

$$|R| = \int_R dx \tag{8}$$

If N independent samples of X of similar distribution are taken and construct the average as

$$\frac{f(X_1) + f(X_2) + \dots + f(X_n)}{N} = \frac{1}{N} \sum_{i=1}^N f(X_i) \tag{9}$$

2.1 Illustration of Monte Carlo based integration with Example

Suppose we have to evaluate the following integral

$$I = \int_a^b f(x) dx \tag{10}$$

In terms of Monte Carlo version, we can write the value of the integral as

$$I = \frac{b-a}{N} \sum_{i=1}^N f(X_i) \tag{11}$$

Where X_i is a random number in the interval (a, b) , that is,

$$X_i = a + (b-a)U, \quad 0 < U < 1 \tag{12}$$

For a two dimensional integral

$$I = \int_a^b \int_c^d f(X, Y) dX dY \tag{13}$$

we can write the Monte Carlo version as

$$I = \frac{(b-a)(d-c)}{N} \sum_{i=1}^N f(X_i, Y_i), \tag{14}$$

where

$$X_i = a + (b-a)U^1, 0 < U^1 < 1 \tag{15}$$

$$Y_i = c + (d - c)U^2, 0 < U^2 < 1 \tag{16}$$

Therefore, we can write the following algorithm to evaluate an integral

- 1) Pick n randomly distributed points x_1, x_2, \dots, x_n in the interval [a,b].

- 2) Determine the average value of the function,
$$\langle f \rangle = \frac{1}{n} \sum_{i=1}^n f(x_i) \tag{17}$$

- 3) Compute the approximation to the integral
$$\int_a^b f(x) dx = (b-a) * \langle f \rangle \tag{18}$$

- 4) An estimate for the error is

$$\approx (b-a) \sqrt{\frac{\langle f^2 \rangle - \langle f \rangle^2}{n}}, \tag{19}$$

where $\langle f^2 \rangle = \frac{1}{n} \sum_{i=1}^n f^2(x_i)$

Example:

Suppose we have to evaluate the integral:

$$I = \int_2^5 f(x) dx = \int_2^5 x^2 dx \tag{20}$$

The value of the $\int_2^5 x^2 dx$, for n = 1000 is obtained as 39.7858, whereas the exact answer of this integral is 39. So, the numerical error produced is equal to 0.7858, which can be reduced by increasing the more number of sample points within the domain of integration. It is a fact that the error in the result will be reduced with the increase of the sample size.

2.2 Approximation of a Double Integral Using Crude Monte Carlo

The Monte Carlo method can be used to numerically approximate the value of a double integral. For a function of two variables the steps are:

- 1) Pick n randomly distributed points

$\{(x_i, y_i) \mid i = 1, 2, \dots, n\}$ in the rectangle [a, b] x [c, d].

- 2) Determine the average value of the function,

$$\langle f \rangle = \frac{1}{n} \sum_{i=1}^n f(x_i, y_i) \tag{21}$$

- 3) Compute the approximation to the integral

$$\int_a^b \left(\int_c^d f(x, y) dy \right) dx \approx (b-a)(d-c) \langle f \rangle \tag{22}$$

- 4) An estimate for the error in Monte Carlo integration is written as

$$\approx (b-a) * (d-c) \sqrt{\frac{\langle f^2 \rangle - \langle f \rangle^2}{n}},$$

where $\langle f^2 \rangle = \frac{1}{n} \sum_{i=1}^n f^2(x_i, y_i)$ (23)

Using this code, the approximate value of the integral

$$\int_0^{5/4} \left(\int_0^{5/4} (4 - x^2 - y^2) dy \right) dx \approx (b-a) * (d-c) * \langle f \rangle =$$

4.5818, where n = 2500 is taken into account. Exact answer of this integration is 4.62. Thus error estimated as 0.04.

3.0 Analytical Expression of Gamma Photon Flux

Analytical expression of gamma photon flux for extended source shield geometry is based on point-kernel technique. Shielding calculation on the basis of point kernel technique is carried out using standard point kernel codes. Therefore, a short literature survey on the point kernel codes is presented below.

There are many codes in wide use that are based on the point-kernel technique. In these codes a distributed source is decomposed into small but finite elements and the dose at some receptor point from each element is computed using the un-collided dose kernel and a buildup factor based on the optical thickness of material between the source element and the receptor. The results for all the source elements are then added together to obtain the total dose. Some that have been widely used are Micro-Shield [13], the QAD series [14], and QAD-CG [15], MORSE [16], QUADMOD [17], G3 [18], ISOSHLD [19] and IGSIELD [20]

Self-absorbing I) cylindrical volume source and II) spherical volume source geometry have been taken into account to illustrate the Monte Carlo approach based evaluation of the complex integral, frequently encountered in radiation shielding. The algorithm has been incorporated in a FORTRAN 90 code to solve these integrals using Monte Carlo method.

I) In a self-absorbing cylindrical source the un-collided flux in the lateral direction at P is

$$\Phi = \frac{S_v}{4\pi} \int_0^v \frac{e^{-\mu x}}{r^2} dv \tag{24}$$

$$= \frac{S_v}{2\pi} \int_0^h dz \int_0^R \rho d\rho \int_0^\pi \frac{e^{-\mu_s x}}{\rho^2 + b^2 + z^2 - 2b\rho \cos\phi} d\phi \quad (25)$$

where $x = x' \sec\psi$. From Fig.1 we can write $x' = FE$ and $x = DE$.

$$x = (PB - PC) \sec\psi \quad (26)$$

$$\sec\psi = \frac{PD}{PB} = \frac{\sqrt{\rho^2 + b^2 + z^2 - 2b\rho \cos\phi}}{\sqrt{\rho^2 + b^2 - 2b\rho \cos\phi}} \quad (27)$$

$$PC = b \cos\alpha - \sqrt{\rho^2 + b^2 - 2b\rho \cos\phi} \quad (28)$$

Since $(b - R) < PC < b \cos\alpha$ and since

$$\cos\alpha = \frac{b - \rho \cos\phi}{\sqrt{\rho^2 + b^2 - 2b\rho \cos\phi}} \quad (29)$$

The final expression for the self-absorption distance x in the material comprising the source takes the form

$$x = \left[\frac{\rho^2 - b\rho \cos\phi + \sqrt{(\rho^2 + b^2 - 2b\rho \cos\phi)R^2 - (b\rho \sin\phi)^2}}{\rho^2 + b^2 - 2b\rho \cos\phi} \right] \times \sqrt{z^2 + \rho^2 + b^2 - 2b\rho \cos\phi} \quad (30)$$

Now introducing the following dimensionless variables:

$$m = \frac{\rho}{R}, \quad n = \frac{z}{R}, \quad k = \frac{h}{R}, \quad p = \frac{b}{R} \geq 1.25 \quad (31)$$

We can write the following expression has the form,

$$\Phi = \frac{S_v R}{2\pi} G(k, p, \mu_s R, b_1 = 0) \quad (32)$$

$$G(k, p, \mu_s R, b_1 = 0) = \int_0^k \int_0^\pi \int_0^1 \left[\frac{mdm(d\phi)dn}{n^2 + m^2 + p^2 - 2mp \cos\phi} \right] \times I \quad (33)$$

$$I = \exp \left\{ \frac{\mu_s R (n^2 - mp \cos\phi + \sqrt{n^2 + p^2 - 2mp \cos\phi} - (mp \sin\phi)^2) \times \sqrt{n^2 + m^2 + p^2 - 2mp \cos\phi}}{n^2 + p^2 - 2mp \cos\phi} \right\} \quad (34)$$

With slab shield $b_1 = \mu_1 t$ where t = thickness of the shield. For this slab shield one has to introduce the factor $e^{-\mu_1 y}$

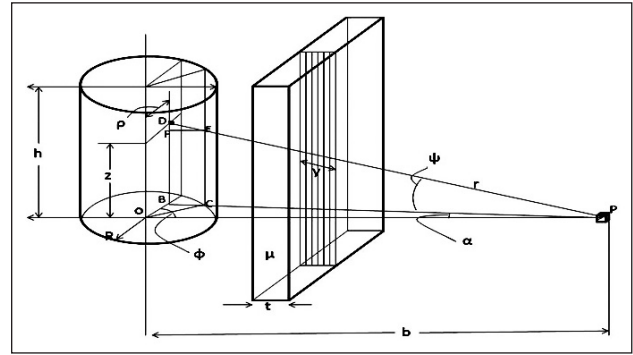


Figure-1: Geometry for self-absorbing cylindrical volume source with slab shield at side

Where, $y = y(z, \rho, \phi)$

$$= t \cdot \sec\alpha \cdot \sec\psi = t \cdot \frac{\sqrt{z^2 + \rho^2 + b^2 - 2b\rho \cos\phi}}{b - \rho \cos\phi} \quad (35)$$

Thus in the case of a shielded self-absorbing cylindrical source, the exact formula for the attenuation function of a flux in the lateral direction has the form

$$\Phi = \frac{S_v R}{2\pi} G(k, p, \mu_s R, b_1) \quad (36)$$

and

$$G(k, p, \mu_s R, b_1) = \int_0^k \int_0^\pi \int_0^1 \left[\frac{mdm(d\phi)dn}{n^2 + m^2 + p^2 - 2mp \cos\phi} \right] \times \left[I + \frac{b_1}{p - m \cos\phi} \right] \quad (37)$$

Thus the analytical expression of the attenuation function contains a function $G(k, p, \mu_s R, b_1)$ which is in integral form. Monte Carlo method of integration technique has been applied to evaluate $G(k, p, \mu_s R, b_1)$.

II) In case of spherical self absorbing volume source (Figure-2) with slab shield, the flux can be expressed using the attenuation function $G_v(p, \mu_s R, \mu_1 t)$ in the formula.

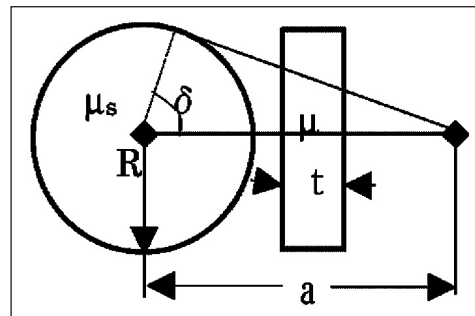


Figure-2: Geometry for self-absorbing spherical volume source with slab shield at side

The un-collided flux in the lateral direction at the detector point is given as

$$\Phi = \frac{S_v R}{\pi} G_v(p, \mu_s R, \mu t) \tag{38}$$

Now introducing the following dimensionless variables:

$$m = \frac{r}{R}, \quad p = \frac{a}{R} \tag{39}$$

Here r , θ and ϕ are respectively the radius, polar angle and azimuthal angle in spherical co-ordinates.

$$G_v(p, \mu_s R, \mu t) = \int_0^1 \int_0^{2\pi} \int_0^\pi \frac{m^2 \cos\theta \, dm \, d\theta \, d\phi}{m^2 + p^2 - 2mp \cos\theta \cos\phi} \exp-(A+B) \tag{40}$$

Where,

$$A = \mu t \frac{\sqrt{m^2 + p^2 - 2mp \cos\theta \cos\phi}}{p - m \cos\theta \cos\phi}$$

and,

$$B = \mu_s R \frac{m^2 - mp \cos\theta \cos\phi + \sqrt{m^2 + p^2 - 2mp \cos\theta \cos\phi} - m^2 p^2 (1 - \cos^2\theta \cos^2\phi)}{\sqrt{m^2 + p^2 - 2mp \cos\theta \cos\phi}} \tag{41}$$

Monte Carlo method of integration technique has been applied to evaluate $G_v(p, \mu_s R, \mu t)$.

4.0 Results and Discussions

Monte Carlo method of integration technique has been adopted to evaluate the value G (in case of cylindrical source) for various values of b_1 , p , k and $\mu_s R$. Results are as shown in Table-1. It can be seen that percent error in the numerical value compared to literature [7] is mostly less than 5%. Only in three cases it is more than 5%, but in overall cases it is less than 10%. The literature values of the function is limited for few values of this function parameters $(k, p, \mu_s R, b_1)$, in case of shielding design there are no limitations on these parameters to evaluate the G function.

At the design stage of shielding the values of these parameters will be changing according to the problem. Therefore, the Monte Carlo based numerical integration technique will be very much helpful to calculate any values of the G function parameters $(k, p, \mu_s R, b_1)$ without any limitations

and the accuracy will be also within the acceptable limits.

Table 1: Evaluated G Function and Its Error

b1	p	k	$\mu_s R$	G	G	Error (%)
				(Simulated)	(Literature)	
2	1.25	1	5	1.10E-02	1.08E-02	1.9
2	1.25	1	10	5.46E-03	5.27E-03	3.5
2	1.25	3	5	1.08E-02	1.09E-02	1.0
2	1.25	3	10	5.34E-03	5.27E-03	1.2
2	1.25	5	5	1.06E-02	1.09E-02	2.0
2	1.25	5	10	5.38E-03	5.27E-03	2.0
2	3	1	5	3.29E-03	3.27E-03	0.8
2	3	1	10	1.71E-03	1.65E-03	3.3
2	3	3	5	5.34E-03	5.31E-03	0.6
2	3	3	10	2.69E-03	2.61E-03	3.2
2	3	5	5	5.47E-03	5.46E-03	0.1
2	3	5	10	2.73E-03	2.67E-03	2.4
4	1.25	1	5	9.81E-04	9.22E-04	6.4
4	1.25	1	10	4.84E-04	4.44E-04	9.0
4	1.25	3	5	9.50E-04	9.23E-04	3.0
4	1.25	3	10	4.78E-04	4.34E-04	10.0
4	1.25	5	5	9.38E-04	9.23E-04	1.7
4	1.25	5	10	4.77E-04	4.34E-04	9.9
4	5	1	5	1.54E-04	1.53E-04	0.6
4	5	1	10	7.91E-05	7.71E-05	2.6
4	5	3	5	3.22E-04	3.20E-04	0.6
4	5	3	10	1.63E-04	1.59E-04	2.5
4	5	5	5	3.56E-04	3.55E-04	0.5
4	5	5	10	1.79E-04	1.75E-04	2.2
20	3	1	5	2.51E-11	2.51E-11	0.3
20	3	1	10	1.27E-11	1.26E-11	1.1
20	3	3	5	2.60E-11	2.63E-11	1.1
20	3	3	10	1.29E-11	1.30E-11	1.4
20	3	5	5	2.54E-11	2.63E-11	3.1
20	3	5	10	1.25E-11	1.30E-11	3.8
20	10	1	5	4.04E-12	4.01E-12	0.6
20	10	1	10	2.05E-12	2.00E-12	2.5
20	10	3	5	9.07E-12	9.01E-12	0.7
20	10	3	10	4.58E-12	4.48E-12	2.4
20	10	5	5	1.03E-11	1.03E-11	0.6
20	10	5	10	5.19E-12	5.08E-12	2.1

During the calculation of the G function a study has been done on the distribution (Figure-3 & Figure-4) of the variance with various iterations up to 10^6 . It is seen that as the iteration increased the variance of this evaluated function gets more stable. An iteration step between 5×10^5 and 10^6 will give an exact estimate of this function while designing shield for a nuclear reactor.

Table-2: Evaluated $G_v(p, \mu_s R, \mu t)$ Function and Its Error

a/R	μt	G_v literature	G_v evaluated	Error (%)	G_v literature	G_v evaluated	Error (%)
$\mu_s R$		4	4		10	10	
1	0	3.39E-01	0.334095	1.5	1.49E-01	0.136824	8.3
1.25	0	1.51E-01	0.15129	0.5	6.27E-02	6.27E-02	0.1
1.25	3	3.88E-03	3.91E-03	0.8	1.58E-03	1.60E-03	1.2
1.25	5	3.84E-04	3.87E-04	0.9	1.54E-04	1.57E-04	2.1
1.5	1	3.07E-02	3.07E-02	0.0	1.26E-02	1.26E-02	0.1
1.5	10	1.47E-06	1.48E-06	0.4	5.91E-07	5.96E-07	0.8
2	1	1.74E-02	1.75E-02	0.1	7.15E-03	7.18E-03	0.3
2	5	2.46E-04	2.46E-04	0.1	9.99E-05	1.00E-04	0.5
2	10	1.24E-06	1.24E-06	0.0	5.02E-07	5.04E-07	0.3
3	3	9.92E-04	9.95E-04	0.3	4.07E-04	4.09E-04	0.5
3	5	1.27E-04	1.27E-04	0.2	5.22E-05	5.23E-05	0.2
3	10	7.52E-07	7.51E-07	0.1	3.05E-07	3.07E-07	0.6
5	1	2.80E-03	2.80E-03	0.0	1.15E-03	1.15E-03	0.2
5	3	3.71E-04	3.72E-04	0.1	1.52E-04	1.53E-04	0.6
10	0	1.91E-03	1.91E-03	0.1	7.83E-04	7.85E-04	0.3
10	1	7.01E-04	7.00E-04	0.2	2.89E-04	2.88E-04	0.1
10	3	9.42E-05	9.43E-05	0.0	3.87E-05	3.88E-05	0.3

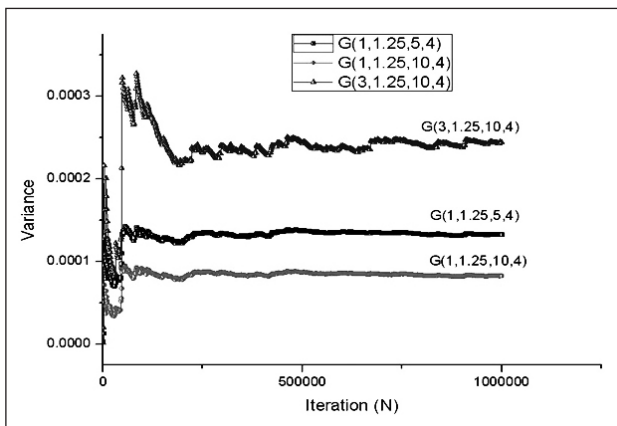


Figure-3: Variance distributions of the 'G' functions with various iterations.

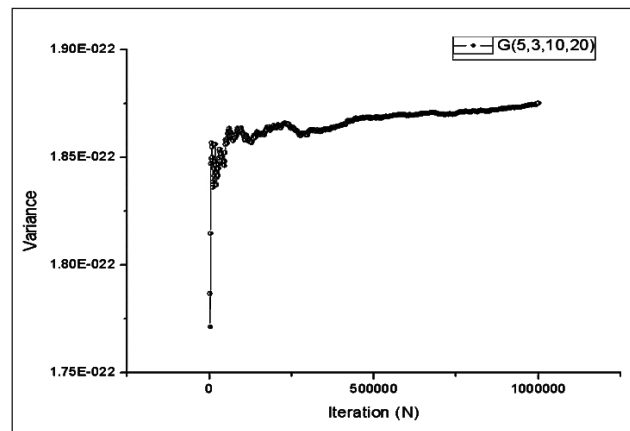


Figure-4: Variance distribution of the 'G' functions with various iterations.

The variance of the function $G(5,3,10,20)$ (Figure-4) is very less ($\sim 10^{-22}$) compared to the Fig-3 ($\sim 10^{-5}$), so different figures are employed here for the distributions of variances with various iteration steps.

In case of the spherical self absorbing volume source with shield the value of $G_v(p, \mu_s R, \mu t)$ for various values of b_1 , p , k and $\mu_s R$ are as given in Table-2. Here 10^6 iteration steps have been considered to get these values. The values obtained are compared with the literature [21] and it has been found that

except only one value all the results are in line with the literature value. The error is less than 5% in most of the results obtained using the Monte Carlo method in FORTRAN 90 language.

References

1. Shultis JK, Faw RE. Radiation shielding. Upper Saddle River, New Jersey: Prentice Hall; 1996.
2. Duderstadt JJ, Martin WR. Transport theory. New York: Wiley; 1979
3. Bureau of Radiological Health. Radiological health handbook. Rockville, Maryland: US Department of Health

- Education and Welfare, Public Health Service, Food and Drug Administration; 1970.
4. National Council on Radiation Protection and Measurements, Radiation protection for Particle Accelerator facilities, Bethesda, MD: NCRP; Report No. 144; 2003.
5. National Council on Radiation Protection and Measurements, Structural shielding design for medical x-ray imaging facilities, Bethesda, MD: NCRP; Report No. 147; 2004.
6. Jaeger RH. Engineering compendium on radiation shielding. Vol I, shielding fundamentals and methods. New York: Springer-Verlag; 1968.
7. Jaeger RH. Engineering compendium on radiation shielding. Vol II, shielding materials. New York: Springer-Verlag; 1975.
8. Rockwell T, III. Reactor shielding design manual. Princeton, NJ: D. Van Nostrand; 1956.
9. Goldstein H. Fundamental aspects of reactor shielding. Reading, MA: Addison-Wesley; 1959.
10. American Nuclear Society. American national standard gamma-ray attenuation coefficients and buildup factors for engineering materials. La Grange Park, IL: American National Standards Institute, American Nuclear Society; ANSI/ANS-6.4.3-1991; 1991.
11. American Nuclear Society. American national standard nuclear analysis and design of concrete radiation shielding for nuclear power plants. La Grange Park, IL: American National Standards Institute, American Nuclear Society; ANSI/ANS-6.4-1997; 1997.
12. Capo MA. Polynomial approximation of gamma-ray build-up data to shield design. Washington, DC: General Electric Corp., Atomic Products Division; U.S. AEC Report APEX-510; 1959.
13. Negin CA, Worku G. Microshield v. 5 user's manual. Rockville, MD: Grove Engineering; 1998.
14. Malenfant RE. QAD: A series of point kernel general-purpose shielding programs. Los Alamos, NM: Los Alamos National Laboratory; LA-3573; 1967.
15. Cain VR. A users manual for QAD-CG, the combinational geometry version of the QAD-P5A point kernel shielding code. San Francisco, CA: Bechtel Power Corp., Report NE007; 1977.
16. Cain VR, Emmett MV. BREESE-II: Auxiliary routines for implementing the albedo option in the MORSE Monte Carlo code. Oak Ridge, TN: Oak Ridge National Laboratory; ORNL/TM-6807; 1979.
17. Price JH, Blattner WGM. Utilization instructions for QADMOD-G. Fort Worth, TX: Radiation Research Assoc., Inc.; RRA-N7914; 1979. Available from RSICC as CCC565/QADMOD-GP.
18. Malenfant RE. G3: A general purpose gamma-ray scattering code. Los Alamos, NM: Los Alamos National Laboratory; LA-5176; 1973. Available from RSICC as CCC-564/G33-GP; 1990.
19. Engle RL, Greenberg J, Hendrickson NM. ISOSHLDD – A computer code for general purpose isotope shielding analysis. Richland, WA: Battelle Northwest Laboratory; BNWL-236; 1966.
20. K.V. Subbaiah, R. Sarangapani, "IGSHIELD: A new interactive point kernel gamma ray shielding code", Annals of Nuclear Energy, vol. 35, (2008) 2234–2242.
21. Hideo EZURE, "Tabulation of Simplified Shielding Formulas", Journal of Nuclear Science and Technology, 39:8, 885-892, 2002.

Ageing Studies on Irradiation Induced Degradation of Graphite Reflector of Cirus Nuclear Research Reactor

Rakesh Ranjan*, S. Bhattacharya, P.V. Varde, Y.S. Rana, G.K. Mallik, V.D. Alur, S. Jeyakumar

Bhabha Atomic Research Centre, Mumbai, India

*Email: ranjanr@barc.gov.in

Abstract

40 MW (Thermal) Research reactor Cirus is located at Bhabha Atomic Research Centre, Mumbai, India. The reactor used natural Uranium metal fuel, heavy water moderator, light water coolant and graphite reflector. It was operated from year 1960 to 2010. From year 1997 to 2003, the reactor was under refurbishment. Currently the reactor has been defueled, spent fuels have been reprocessed and heavy water has been removed from the reactor. A deferred dismantling strategy has been selected for its decommissioning. Preliminary activities in this regard has been started. Various properties of irradiated graphite are being analysed to assess condition of graphite to select the best course of action during decommissioning which includes options such as re-use and / or disposal.

Key words – graphite, Wigner energy, reflector, lattice, neutron flux

1. Introduction

Cirus research reactor was shut down in 2010 after logging over 45 years of service life. This reactor had seen major refurbishing based on ageing studies performed as part of life extension programme. This data and experience generated during ageing studies and refurbishment programme can significantly contribute to future need of ageing assessment and residual life prediction for core

components of research reactors. An IAEA CRP on “Ageing Data on Corrosion and Irradiation Induced Degradation of In-Core Components of Research Reactor Cirus” was initiated and studies related to Graphite were identified as a major component of the programme. This report describes about stored energy in irradiated graphite and physical condition of Graphite blocks indicating the extent of degradation.

1.1 Brief Description of Cirus Reactor

Cirus is situated at Bhabha Atomic Research Centre, Mumbai, India. It is a 40 MW (Thermal) natural Uranium metal fuelled, heavy water moderated, light water cooled research reactor commissioned in July 1960. The maximum thermal neutron flux of Cirus reactor is 6.6×10^{13} n/cm²-sec. Graphite has been used as reflector. Reactor vessel is an Aluminium tank of 267 cm diameter and 320 cm height. The graphite reflector is arranged in the form of two concentric cylinders around the reactor vessel. The annular gap between the inner and outer graphite reflectors can accommodate irradiation assemblies. Ventilation air passing

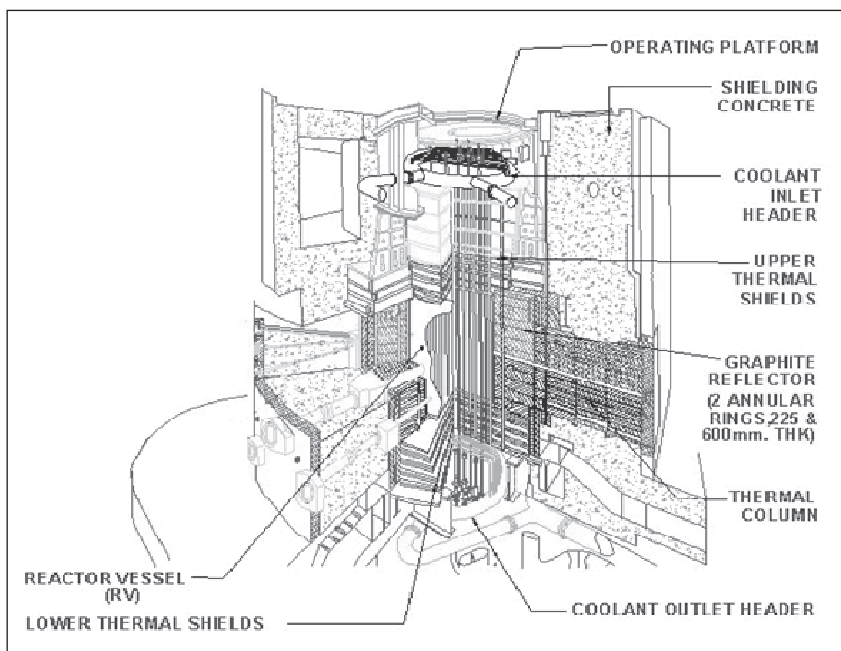


Fig. 1: Cirus Reactor structure cross section

through the reactor structure removes the heat produced in such irradiation assemblies as well as the structural components including graphite reflectors. Thermal shields are provided around the reflector and above and below the reactor vessel. The RV, the reflector and the side thermal shields are surrounded by 8 ft. (24.4 m) thick high density concrete.

2. Neutron Flux Profile

At the rated power of 40 MW, the maximum neutron fluxes at the various structural components vary in the range $3.2E+12$ n/cm²/sec for the neutron energy above 1 MeV to $6.5E + 12$ n/cm²/sec for neutron energy below 0.4 eV. The estimated region mean slow neutron flux values at 40 MW in the radial direction varied in the range $5.4E + 13$ n/cm²/sec in the Calandria (fast flux ratio=0.61) to $2.7E+06$ n/cm²/sec at the cast iron side thermal shield (fast flux ratio = 72). The estimated region mean slow neutron flux values at 40 MW in the axial direction varied in the range $3.6E +06$ n/cm²/sec in the bottom base plate (fast flux ratio = 260), $3.9E+13$ n/cm²/sec in the Calandria region and to $1.4E+08$ n/cm²/sec at the top steel thermal shield (fast flux ratio = 256).

GRAPHITE REFLECTOR: The graphite reflector of Cirus consists of two co-axial cylindrical structures

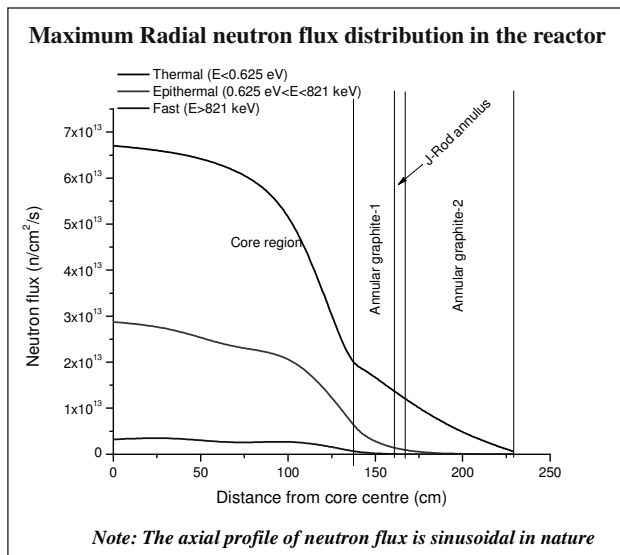


Fig. 2: Flux Profile in Reactor

of 330 cm height placed around the reactor vessel and separated by an annular gap of 2½" (6.35 cm), called J-rod annulus, between the inner and outer structures. The inner reflector has a thickness of 23 cm and weight of about 10 Tons, while the outer one has a thickness of 61 cm and weight of about 36 Tons. This graphite has been subjected to intense neutron

irradiation. The volume averaged neutron flux values (neutron energy > 500 eV) at rated reactor power are estimated to be $3.4E+12$ n/cm²/sec for the inner graphite reflector and $5.0E+11$ n/cm²/sec for the outer graphite reflector. The corresponding neutron fluence after 31 years of operation in year 1991 were $2.3 E+21$ n/cm² for the inner reflector and $3.4E+20$ n/cm² for the outer reflector.

For cooling of graphite, ventilation air is made to pass through the annular space between the inner and outer graphite structures, known as J-rod annulus. Under normal operating condition of ventilation system, the graphite reflector is cooled with 18000 cfm (106000 m³/h). Under off-site (Class-1V) power failure condition, the ventilation system with class-III supply, provides cooling to the graphite reflector at flow rate of 12000 cfm (7000 m³/h). The measured maximum operating temperature of the inner reflector at 40 MW is about 150° C and that of the outer reflector is about 100° C. When graphite is irradiated, crystal lattice defects are produced due to displacement of atoms from their normal position in the lattice leading to stored Wigner energy. The energy stored due to irradiation is a function of neutron energy, neutron irradiation received and operating temperature during irradiation. Thermal conductivity of graphite also decreases with increase of stored energy. When irradiated graphite temperature is raised by external heating or by the heat generated due to irradiation, the displaced atoms can get back to their vacant positions in the lattice, thus causing release of stored energy. The energy release depends on the temperature attained by the irradiated graphite and stored energy level. During irradiation when stored energy is getting accumulated, concurrent annealing of graphite also occurs.

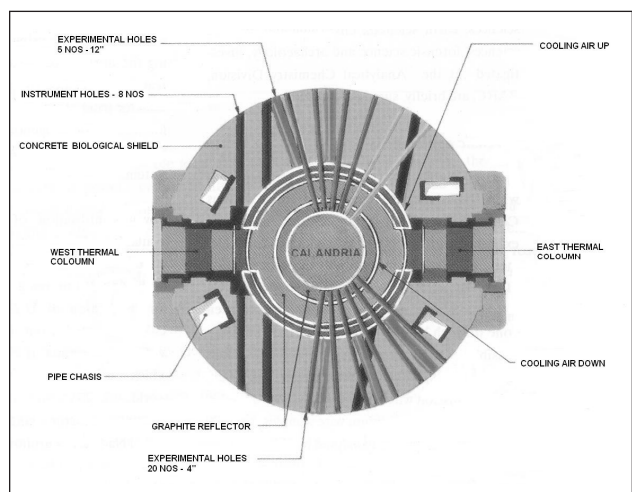


Fig 3: Simplified plan of Cirus reactor structure

3. Graphite Reflector Assembly:

There are also two thermal column on east and west side of reactor called EAST Thermal Column and WEST Thermal Column. Moderator used in thermal column is graphite. Thermal column is a source of thermal neutrons. Each thermal column has a central hole, which is plugged by reactor grade graphite plugs. The inner plug is made of two sections and extends from the inner face of the inner reflector up to the outer face of the fixed thermal column. The outer assembly is made of three sections and extends throughout the entire length of the removable thermal column.

4. Assessment of (Wigner) Stored Energy in Irradiated Graphite Reflector

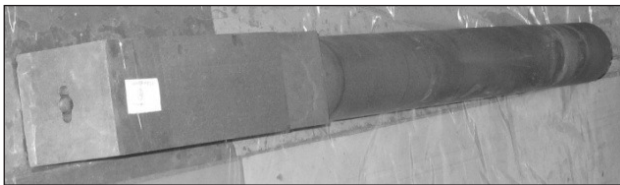


Fig. 4: Inner Plug from I-15 position

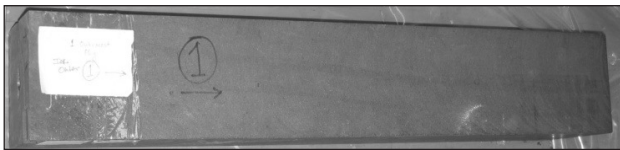


Fig 5: Outer plug (3 nos) from I-15 position

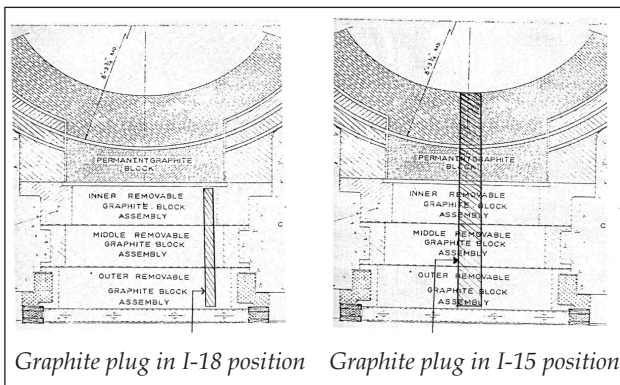


Fig. 6: Arrangement of Graphite in Thermal Column and Graphite plugs

A few years prior to the shutdown in 1997 for refurbishment work, the Cirus reactor was operated at 20 MW. It was considered that this could have increased the Wigner energy in the graphite due to decreased concurrent annealing during this period. For measurement of Wigner Energy release by Differential Scanning Calorimetry, sampling was

carried out on reflector graphite plugs that were extracted from mid height location of the east thermal column and west thermal column. These plugs were expected to represent the portion of the reflector, which is subjected to irradiation with maximum neutron fluence and consequently the worst conditions of stored energy. Details of Graphite plugs are as under:

- (a) GR-I: After 37 years of normal operation of CIRUS but at < 20 MW power in its last phases (from I-15 position of thermal column).
- (b) GR-II: After 37 years of usual operation but at <20 MW power in its last phases followed by 1 month operation at > 20 MW power (from I-22 position of thermal column).
- (c) GR-III: After 37 years of usual operation but at <20 MW power in its last phases followed by 1 month operation at >20 MW power and drawn on 18-01-2005 after restarting and operating CIRUS subsequent to its refurbishing. It was essentially the same plug as for GR-1 sampling but with higher service period.
- (d) GR-IV: In 2014, after about 3 ½ years of permanent shut down of reactor, a plug from west thermal column of reactor was removed and samples were prepared for study of Wigner energy, thermal conductivity, specific heat, hardness, XRD and study of lattice structure. This plug has always been in reactor since the beginning but at a lower flux level. The average neutron fluence seen by the plug was estimated to be $1.7 \text{ E}+19 \text{ nvt}$ while the maximum fluence seen by the inner most part of the plug towards core was $4.1 \text{ E}+19 \text{ nvt}$. The fluence seen by the outer most part of the plug was $4.3 \text{ E}+18 \text{ nvt}$. The average gamma fluence in the plug was estimated to be $2.1 \text{ E}+16 \text{ photons/cm}^2$. The maximum value at the incident face was $4.2 \text{ E}+16 \text{ photons/cm}^2$. The block measures $4'' \times 4'' \times 30''$, having contact field 15-20 mR/h.
- (e) GR-V: In 2016, after about 6 years of permanent shut down of reactor, a plug assembly from I-15 position of East thermal column of reactor was removed and samples were prepared for study of Wigner energy, thermal conductivity, specific heat, hardness, etc. The inner plug of this plug assembly had been replaced in January 2005 and was in service for six years till permanent shut down of the reactor. The outer plugs (three nos) remained the old ones. GR-I

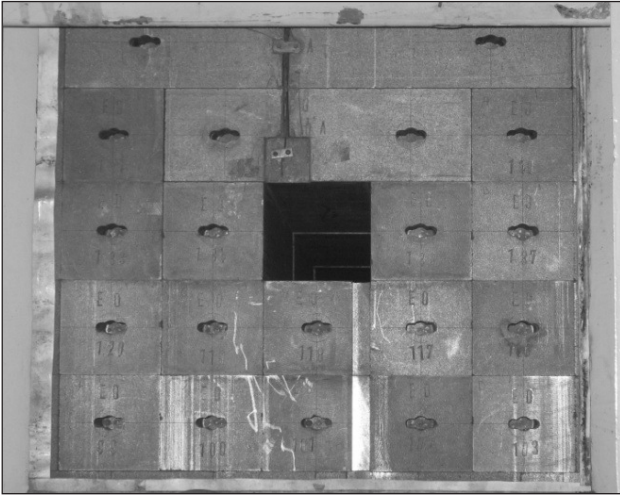


Fig 7: East Thermal Column

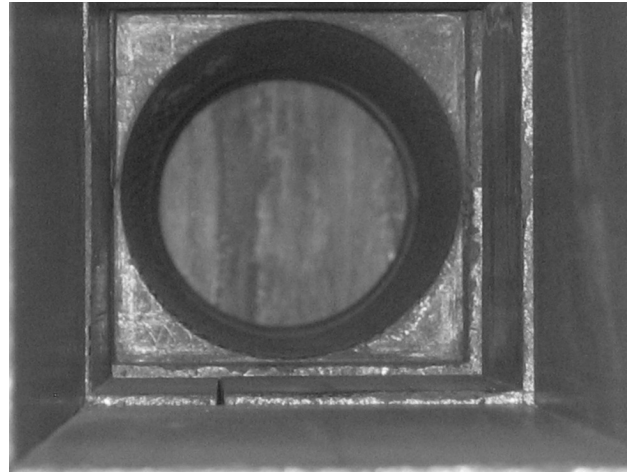


Fig 9: Reactor vessel (within the circle) seen after removal of Graphite plug

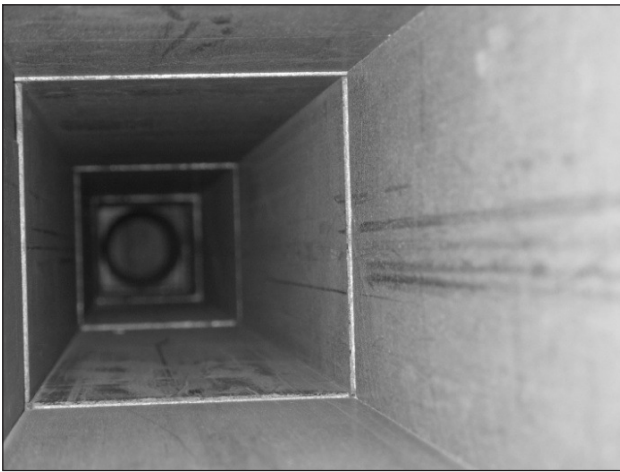


Fig 8: Hole after removing the plugs

sample had earlier been collected from this plug assembly (I-15 position) from the inner plug. The maximum thermal neutron fluence seen by the inner most part of the inner plug towards core was $22.06 \text{ E}+20$ nvt. The thermal neutron fluence seen by the plug at about 90 cm away from the inner most face was $0.75 \text{ E}+20$ nvt. Radiation field on contact at the inner most face was 3 R/hr.

5. Normal Operating Temperatures of Graphite:

The graphite temperature largely depends upon heat flux and flow & temperature of cooling air. It is affected by equilibrium moderator height, moderator temperature, loading in annulus, structural

Table 1: Neutron Flux and Fluence of GR-V Sample

Sr. No.	Distance from inner face of inner plug (cm)	Thermal Neutrons ($E < 0.625 \text{ eV}$)		Epithermal Neutrons ($0.625 \text{ eV} < E < 821 \text{ KeV}$)		Fast Neutrons ($821 \text{ KeV} < E < 20 \text{ MeV}$)	
		Flux ($\times 10^{13}$ n/cm ² /s)	Fluence ($\times 10^{20}$) n/cm ²	Flux ($\times 10^{12}$) n/cm ² /s)	Fluence ($\times 10^{19}$) n/cm ²	Flux ($\times 10^{11}$) n/cm ² /s)	Fluence ($\times 10^{18}$) n/cm ²
1	0	2.88	22.06	4.92	37.69	2.61	19.99
2	5	2.66	20.37	3.28	25.12	1.72	13.17
3	10	2.42	18.53	2.15	16.46	1.11	8.5
4	15	2.17	16.62	1.37	10.49	0.691	5.29
5	20	1.97	15.09	0.964	7.38	0.483	3.7
6	30	1.69	12.94	0.562	4.3	0.266	2.03
7	40	1.32	10.11	0.225	1.72	0.11	0.084
8	50	0.99	7.58	0.0871	0.67	0.0446	0.034
9	60	0.70	5.38	0.0383	0.29	0.0206	0.016
10	70	0.45	3.44	0.0105	0.08	0.00816	0.0063
11	80	0.22	1.71	0.0065	0.05	0.00429	0.0033
12	90	0.098	0.75	0.0040	0.03	0.00169	0.0013

temperatures, incidental water ingress into annulus, etc. Twenty-seven thermocouples were provided for monitoring the temperature of inner graphite reflector (IG) and nine thermocouples for outer graphite reflector (OG). Temperatures varied from 60-150 °C in graphite reflector block. Temperature of graphite in thermal column is <60 °C.

6. Differential Scanning Calorimeter (DSC) Procedure

For the DSC studies, un-irradiated graphite material, obtained from CIRUS, was used as the reference material. The DSC scans were carried out from ambient to 700°C. The results of the first scan were used for Wigner energy calculations. Repeated scans on the irradiated samples did not show any further discernible Wigner energy release. The second run on the same sample was used for blank correction. The parameters chosen for DSC measurement were:

Temperature range of scanning: Ambient to 700°C

Pan Material : Platinum

Sample weight : 30 mg

Environment: Lolar - II Argon at a flow rate of 50 ml / min

Heating programme:- Linear heating rate of 5±0.1°C / min

Table-2 : Wigner Energy Release in Graphite Reflector of CIRUS at different Reactor Operation Period

Sr No.	Distance from RV side end (mm)	Net Wigner Energy (J/g)				
		GR-I	GR-II	GR-III	GR-IV	GR-V
1	0	560.12	543.4	480	--	275.47
2	24	338.58	426.36	352.54	--	--
3	100	259.16	280.06	316.55	--	--
4	150	--	--	--	--	209.96
4	216	292.6	217.36	242.86	--	--
5	306	359.48	246.62	233.12	--	--
6	450	163.02	158.84	162.39	--	--
7	1590	--	--	--	138.83	--
8	1840	--	--	--	236.51	--
9	2060	--	--	--	219.16	--
10	2250	--	--	--	13.71	--
11	2280	--	--	--	15.55	--

Reference material : Un-irradiated graphite of CIRUS

Blank correction : Second DSC scan on the same sample

Calibration: Done using pure Indium standard.

The DCS plots were re-plotted after conversion of the energy release values (in mW) to the units of specific heat (i.e. cal/g/°C or J/g) to give the Wigner energy spectrum.

Cylindrical blanks of 4mm diameter were drilled out from predetermined locations in the graphite plug. Thin wafers for DSC measurements were sectioned using a slow speed diamond wafering wheel. Dry cutting was resorted to, in order to avoid possible errors that would arise due to the entrapped coolant in the samples. For DSC measurements, 2mm thick wafer samples were sectioned from the cylindrical blank of 4mm diameter. This method of sampling ensured perfectly flat and parallel surfaces with smooth finish. The sampling tools and the procedure were designed to restrict the temperature rise, at the sampling site, not more than 1°C during cutting operation. This was essential since any increase in sample temperature could lead to uncertainties in the stored energy measurements.

7. Linear Heating Experiments on Samples From Graphite Plug GR-1

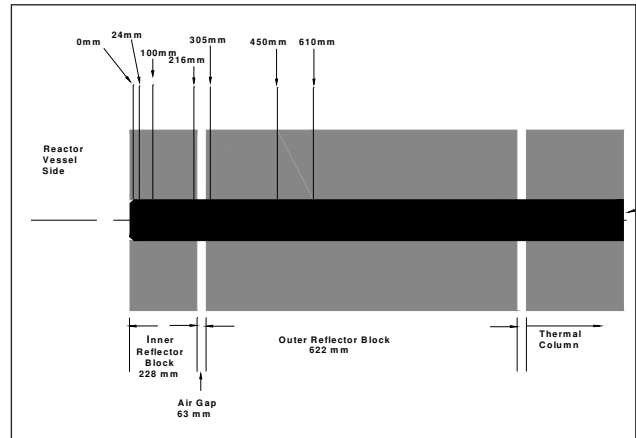


Fig 10: Graphite plug sampling plan for Wigner energy release studies

The DSC plots gave the results of energy release in the units of mW (mcal/s). These values were re-plotted after converting to the units of specific heat, J/g/°C (cal/g/°C) to give the Wigner energy spectrum.

From the Wigner energy release spectra of the different samples from graphite plug GR-I it could

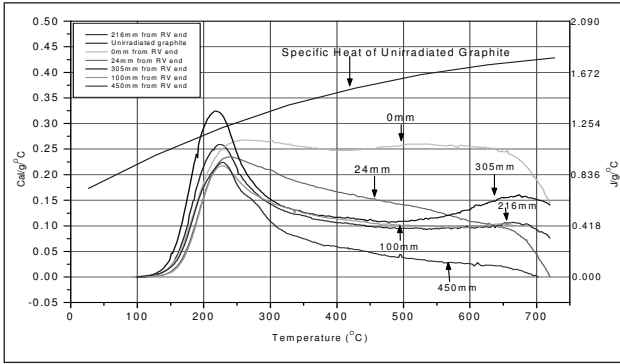


Fig 11: Wigner energy spectra of the samples from irradiated graphite plug (GR-I) of CIRUS after about 37 years of reactor operation.

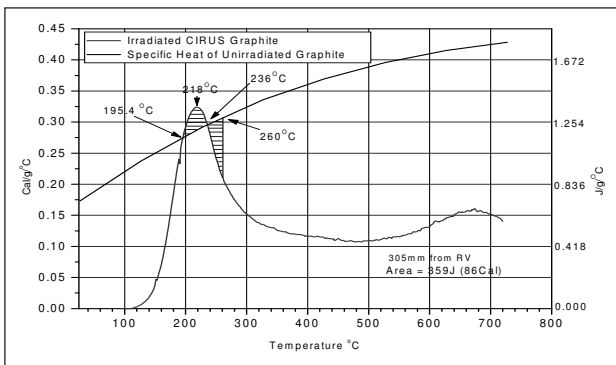


Fig 12: Wigner energy spectrum, of sample at 305mm from RV side end of irradiated graphite plug (GR-I) of CIRUS after 37 years of service, showing spontaneous temperature rise during linear heating

be seen that all the Wigner energy spectra, except the one for the sample from 305mm distance from the RV side end of the plug, are seen to lie below the specific heat curve. The Wigner energy spectrum of the sample from 305mm location is seen to be crossing the specific heat curve at a temperature of 195°C. From equivalent area treatment, it was seen that this would lead to a sudden temperature increase to 260°C.

8 Isothermal Annealing Studies On Samples From Graphite Plug GR-I

Isothermal annealing experiments were carried out on freshly prepared samples from different locations on the plug. Step heating studies were carried out in temperature steps of 10°C from 110 to 170°C as per the predetermined temperature program. This experiment was to ascertain whether there was any energy release at low temperatures (in the range of 100 - 170 °C) and to find out the total energy release up to 450°C. Extended period isothermal annealing studies were also carried out at 120°C for 12 hours with a predetermined temperature program.

Results of step heating experiments indicated measurable energy release of the irradiated graphite even during short time (2 hours) isothermal annealing, in such low temperature regimes as 100-170°C. The results of 12 hours isothermal annealing experiments at 120°C have confirmed the possibility of partial irradiation annealing of the Wigner energy in CIRUS reflector graphite by brief periods of operating temperatures higher than the corresponding temperatures at 20 MW reactor operations.

9. Studies on the Graphite Plug (GR-II) After High Power Operation of CIRUS

Subsequent to CIRUS reactor operation at power level higher than 20 MW for a brief period of about one month in September 1997, a graphite plug (GR-II), that was considered similar in all respects to the plug GR-I, was removed for detailed Wigner energy estimation. Evaluation of the stored energy release was carried out, using the same DSC scan parameters as used for the plug GR-I.

The significant feature of the Wigner energy spectrum of the samples from GR-II is that there

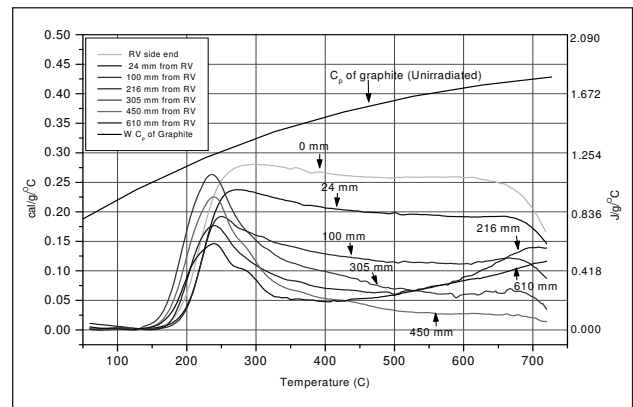


Fig 13: Wigner energy spectra of the samples from irradiated graphite plug (GR-II) of CIRUS after high power operation of CIRUS.

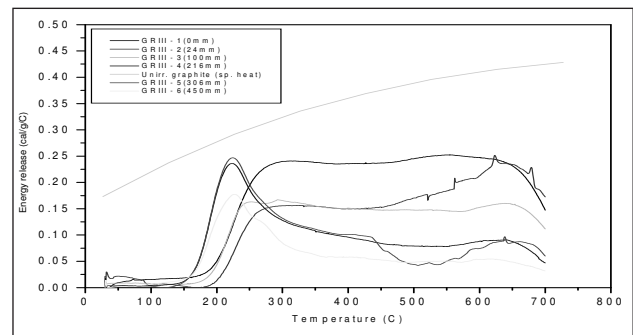


Fig 14: Wigner energy spectra of the samples from irradiated graphite plug (GR-III) after high power operation.

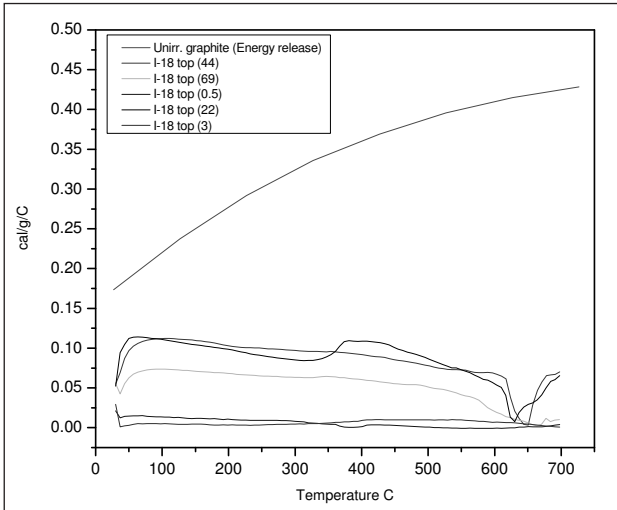


Fig. 15: Wigner energy spectra of the samples (GR IV) from graphite plug from I-18 hole

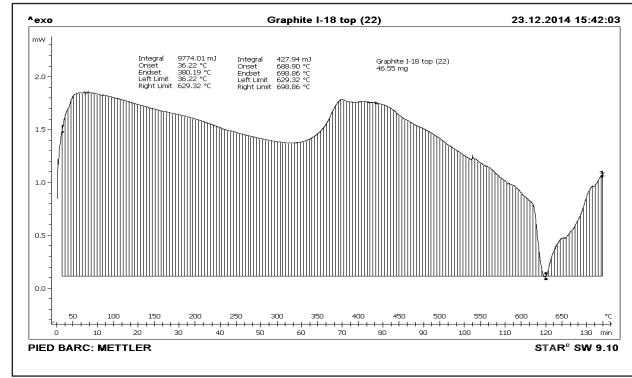


Fig. 18: Wigner energy spectrum of irradiated graphite sample I-18/3

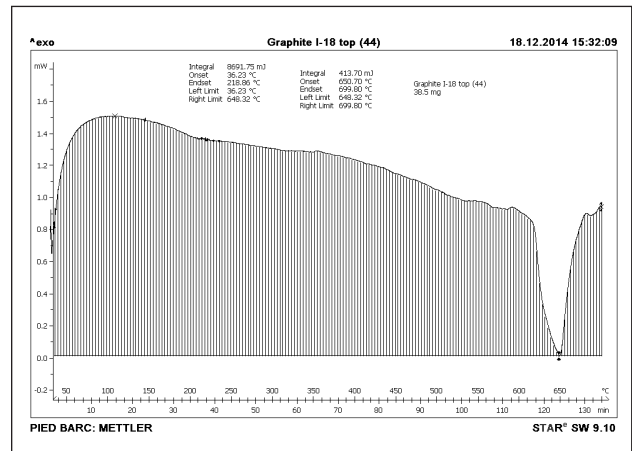


Fig. 19 Wigner energy spectrum of irradiated graphite sample I-18/4

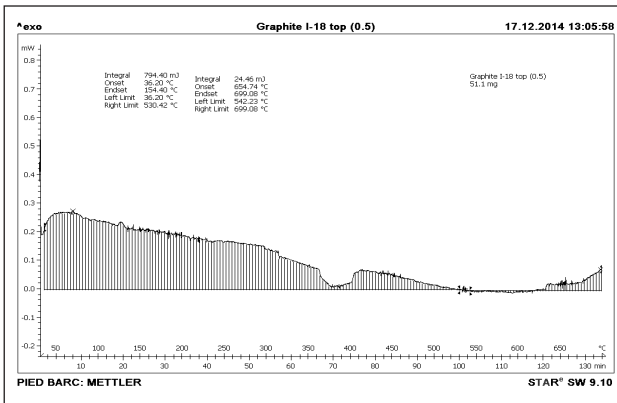


Fig. 16: Wigner energy spectrum of irradiated graphite sample I-18/1

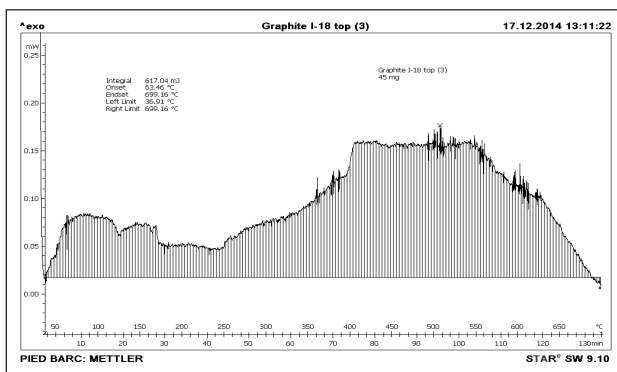


Fig. 17: Wigner energy spectrum of irradiated graphite sample I-18/2

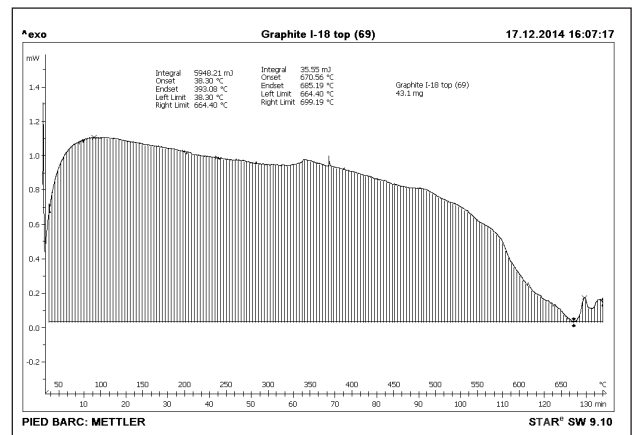


Fig. 20: Wigner energy spectrum of irradiated graphite sample I-18/5

is no location on the plug GR-II where the Wigner energy spectrum crosses the specific heat curve. Whereas, the sample from GR-I showed the Wigner energy spectrum crossing the specific heat curve. This indicates that, as expected, some irradiation

annealing has taken place in the CIRUS graphite due to the high power operation, though the maximum temperature of the graphite was only 120°C.

Experience with Removal of Inner Graphite Plug from Thermal Columns: As inner graphite plugs of

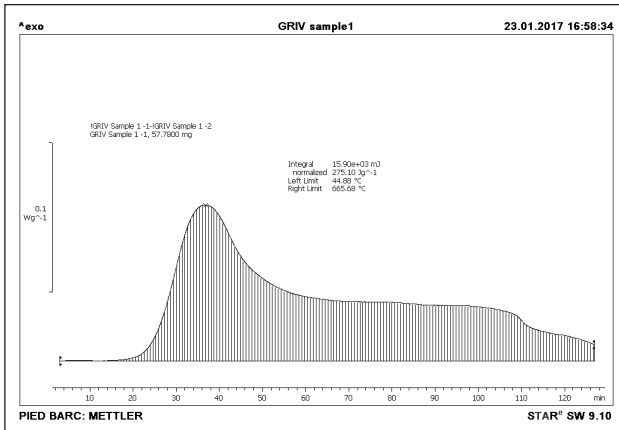


Fig. 21: Wigner energy spectrum of irradiated graphite sample (GR V) from I-15 hole

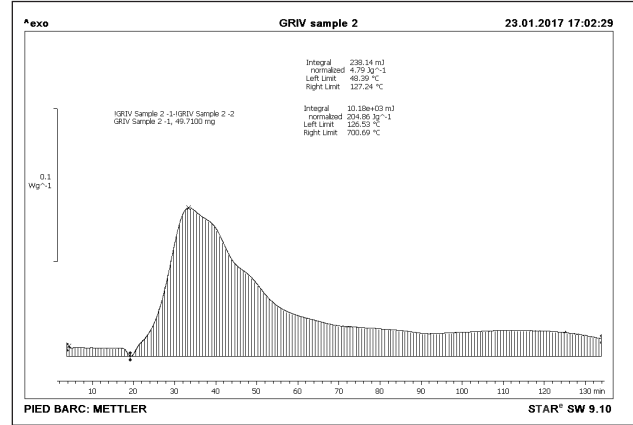


Fig. 22: Wigner energy spectrum of irradiated graphite sample (GR V) from I-15 hole

thermal column positions I-15 and I-22 were extending right up to inner face of inner reflector, they were thought to be the most representative samples as they had been subjected to same neutron flux and other stresses as the inner face of inner graphite. Theoretical estimate of applied force to remove the plugs was made. Factors such as weight of the plug, friction coefficient between mating surfaces, maximum tensile strength of reactor grade graphite, weakest link between two sections, safety factor, etc. were taken into account and a force of about 200 kg was estimated to be enough to take out the plugs. The 90" long outer section of graphite plug from I-15 position was removed on 8.1.97 by simply pulling out. Due care was taken to prevent any vertical displacement of three sections. Maximum field on contact on this section was 2 R/hr. Attempt was made to pull out the inner section of the plug by applying load of 150 kg, however it was unsuccessful. Subsequently, the plug was cleaned at its location near J-rod annulus with liquid nitrogen and air remotely. The tensile force on the plug was made collinear using appropriate tools and it was increased slowly in steps. When a load of about 250 kg was applied, the graphite plug moved out with a jerk. The plug was taken out with due precautions. Maximum radiation field on inside surface of the plug was 7 R/hr. On 01.06.1998, the plug from I-22 position of thermal column was taken out

in similar fashion by applying 220 kg force. Here, in this case cleaning of the plug near J-rod annulus with liquid nitrogen and air was not warranted.

10. Assessment of Physical Condition of Cirus Graphite Blocks:

Graphite blocks seem to be intact and not deformed due to irradiation as they have been subjected to low temperature and damage as corroborated by low Wigner energy. This is further corroborated by i) Straightness of neutron beam lines, ii) Straightness of J-rod holes iii) Straightness of Self-serve (an irradiation facility) carrier tubes, etc. Visual inspection of beam holes by camera in past have not shown any distortion.

References

1. The Canada India Reactor, AECL-1443 (1960)
2. 'Assessment of Radiation Fields from Neutron Irradiated Structural Components of the 40 MW Research Reactor Cirus'. S. Sankaranarayanan and S. K. Sharma, Paper presented at the Advisory Group Meeting on Nuclear Data Requirements for Fission Reactor Decommissioning, September 7-11, 1992, IAEA, Vienna.
3. Cirus-Glorious 50 Years; a book on completion of 50 years of operation of Cirus in year 2010, published by BARC
4. Various internal reports on Cirus ageing studies.
5. Various report from PIED on studies of Wigner Energy in Cirus Graphite plugs
6. Various reports on neutron fluence estimation on structural components of Cirus reactor



SRESA JOURNAL SUBSCRIPTION FORM

Subscriber Information (Individual)



_____	_____	_____	_____
Title	First Name	Middle Name	Last Name
_____		_____	
Street Address Line 1		Street Address line 2	
_____		_____	
City	State/Province	Postal Code	Country
_____	_____	_____	_____
Work Phone	Home Phone	E-mail address	

Subscriber Information (Institution)

Name of Institution/ Library	_____
Name and Designation of Authority for Correspondence	_____
Address of the Institution/Library	_____



Subscription Rates

	Subscription Quantity	Rate	Total
Annual Subscription (in India)	_____	Rs. 15,000	_____
(Abroad)	_____	\$ 500	_____
	_____		_____
	_____		_____

Payment mode (please mark)

Cheque Credit Card Master Card Visa Online Banking Cash De mand Draft

Credit card Number _____



Credit Card Holders Name _____

Credit Card Holde _____



Guidelines for Preparing the Manuscript

A softcopy of the complete manuscript should be sent to the Chief-Editors by email at the address: editor@sresa.org.in. The manuscript should be prepared using 'Times New Roman' 12 font size in double spacing, on an A-4 size paper. The illustrations and tables should not be embedded in the text. Only the location of the illustrations and tables should be indicated in the text by giving the illustration / table number and caption.

The broad structure of the paper should be as follows: a) Title of the paper – preferably crisp and such that it can be accommodated in one or maximum two lines with font size of 14 b) Name and affiliation of the author(s), an abstract of the paper in ~ 100 words giving brief overview of the paper and d) Five key words which indicates broad subject category of the paper. The second page of the paper should start with the title followed by the Introduction

A complete postal address should be given for all the authors along with their email addresses. By default the first author will be assumed to be the corresponding author. However, if the first author is not the corresponding author it will be indicated specifically by putting a star superscript at the end of surname of the author.

The authors should note that the final manuscript will be having double column formatting, hence, the size of the illustration, mathematical equations and figures should be prepared accordingly.

All the figures and tables should be supplied in separate files along with the manuscript giving the figure / table captions. The figure and table should be legible and should have minimum formatting. The text used in the figures and tables should be such that after 30% reduction also it should be legible and should not reduced to less than font 9.

Last section of the paper should be on list of references. The reference should be quoted in the text using square bracket like '[1]' in a chronological order. The reference style should be as follow:

1. Pecht M., Das D, and Varde P.V., "Physics-of-Failure Method for Reliability Prediction of Electronic Components", Reliability Engineering and System Safety, Vol 35, No. 2, pp. 232- 234, 2011.

After submitting the manuscript, it is expected that reviews will take about three months; hence, no communication is necessary to check the status of the manuscript during this period. Once, the review work is completed, comments, will be communicated to the author.

After receipt of the revised manuscript the author will be communicated of the final decision regarding final acceptance. For the accepted manuscript the author will be required to fill the copy right form. The copy right form and other support documents can be down loaded from the SRESA website: <http://www.sresa.org.in>

Authors interested in submitting the manuscript for publication in the journal may send their manuscripts to the following address:

Society for Reliability and Safety
RN 68, Dhruva Complex
Bhabha Atomic Research Centre,
Mumbai - 400 085 (India)
e-mail : editor@sresa.org.in

The Journal is published on quarterly basis, i.e. Four Issues per annum. Annual Institutional Subscription Rate for SAARC countries is Indian Rupees Ten Thousand (Rs. 10,000/-) inclusive of all taxes. Price includes postage and insurance and subject to change without notice. For All other countries the annual subscription rate is US dollar 500 (\$500). This includes all taxes, insurance and postage.

Subscription Request can be sent to SRESA Secretariat (please visit the SRESA website for details)

SRESA's International Journal of
**Life Cycle Reliability
and Safety Engineering**




Contents

Vol. 5

Issue No.4

October-December 2016

ISSN - 2250 0820

- 1. Physics Aspects of Adjuster Rod in Dhruva**
*Tej Singh, Paritosh Pandey, Jagendra Kumar, H. G. Gujar,
P.V. Varde & S. Bhattacharya, (India).....1*
 - 2. Estimation of Fatigue Model Parameters For PLCC Solder
Joints Under Thermal Cycling** 
Rohit Khatri, Diana Denice, Manoj Kumar, P.P.Marathe, (India) ...6
 - 3. Quantification of Functional Failure Probability of a
Passive Safety System** 
Chandrakar A., Nayak A.K., Vinod Gopika, (India)14
 - 4. Numerical Solution of Shielding Integrals Using Monte
Carlo Simulation Method** 
Avijit Das, Tej Singh and P. V. Varde, (India).....25
 - 5. Ageing Studies on Irradiation Induced Degradation
of Graphite Reflector of Cirus Nuclear Research Reactor**
*Rakesh Ranjan, S. Bhattacharya, P.V. Varde, Y.S. Rana,
G.K. Mallik, V.D. Alur, S. Jeyakumar, (India)32*
-